



**INSA** INSTITUT NATIONAL  
DES SCIENCES  
APPLIQUÉES

HAUTS-DE-FRANCE



---

# Numerical analysis of cross-flow reinforced impingement cooling through a U-shaped turbulator

---

Internship report  
By Safae Chargui  
September 2022-January 2023

January 9, 2023

Industrial Tutor: Dr.-Ing. Robin G. Brakmann

University Tutor: Pr.-Dr. Julien Pellé

# **Acknowledgements**

This work is supported by the German Federal Ministry for Economic Affairs and Energy and executed within the DLR Projects InnoCool and FFE+. The present work has been supported by Koral Technologies Srl (Trento, Italy).

# **Engagement de non plagiat**

# Abstract

Impingement cooling offers an efficient usage of cooling air in order to obtain high heat transfer rates. In this study a U-shaped turbulator is installed downstream of the jet hole. This arrangement uses the cross-flow to reinforce the jet by guiding it into the adjacent jet and thus increasing its effective jet Reynolds number. Compared to a smooth channel configuration, the Nusselt number on the target can be increased by 5-16% without a significant change in the pressure loss. This is a purely aerodynamic effect and is not caused by increasing the area of the heat exchanging surface. The geometry represents a generic impingement cooling configuration with a row of nine inline impingement jets. All jets are influenced by a self-induced cross-flow. The jet-to-plate spacing as well as jet pitch are set to 5D and the curved U-shape ribs are installed downstream of the jet on the hole plate. The RANS simulations are performed with the SST turbulence model. The effects of different jet-to-plate spacing, jet Reynolds number as well as rib height, position and shape are investigated numerically. The effectiveness of the U-shaped turbulator is discussed in combination with additional turbulators (from the literature). This paper concludes with a best practice guide for the usage of the U-shaped turbulator in gas turbine cooling designs. A discussion of the manufacturability by Selective Laser Melting is included.

# Résumé

Le refroidissement par impact permet d'utiliser efficacement l'air de refroidissement afin d'obtenir des taux de transfert de chaleur élevés. Dans cette étude, un turbulateur en forme de U est installé en aval de l'orifice du jet. Cet arrangement utilise le flux transversal pour renforcer le jet en le guidant dans le jet adjacent et en augmentant ainsi son nombre de Reynolds effectif. Par rapport à une configuration de canal lisse, le nombre de Nusselt sur la cible peut être augmenté de 5 à 16% sans changement significatif de la perte de pression. Il s'agit d'un effet purement aérodynamique et n'est pas dû à l'augmentation de la surface d'échange de chaleur. La géométrie représente une configuration générique de refroidissement par impact avec une rangée de neuf jets d'impact en ligne. Tous les jets sont influencés par un flux transversal auto-induit. L'espacement entre les jets et les plaques ainsi que le pas des jets sont fixés à  $5D$  et les nervures courbes en forme de U sont installées en aval du jet sur la surface de la plaque. Les simulations RANS sont réalisées avec le modèle de turbulence SST. Les effets des différents espacements entre le jet et la plaque, le nombre de Reynolds du jet ainsi que de la hauteur, de la position et de la forme des nervures sont étudiés numériquement. L'efficacité du turbulateur en forme de U est discutée en combinaison avec d'autres turbulateurs (issus de la littérature). Cet article se termine par un guide des meilleures pratiques pour l'utilisation du turbulateur en forme de U dans les conceptions de refroidissement des turbines à gaz. Une discussion sur la possibilité de fabrication par fusion sélective au laser est incluse.

# Contents

<b>1</b>	<b>Introduction</b>	<b>1</b>
1.1	Turbine Cooling . . . . .	1
1.2	Aim of the work . . . . .	4
1.3	The human aspect during my internship . . . . .	5
1.3.1	Team presentation . . . . .	5
1.3.2	The memories during my internship . . . . .	6
<b>2</b>	<b>Result:ASME paper</b>	<b>10</b>
2.1	Introduction . . . . .	10
2.2	Numerical Setup . . . . .	13
2.2.1	Geometry . . . . .	13
2.2.2	Steady-RANS Simulations . . . . .	13
2.2.3	Convergence and Grid Quality . . . . .	15
2.2.4	Validation . . . . .	16
2.3	Results . . . . .	17
2.3.1	Parameter variation . . . . .	17
2.3.2	Flow Field . . . . .	20
2.3.3	Heat transfer . . . . .	24
2.3.4	Effect of Reynolds number . . . . .	26
2.3.5	Combination with other features . . . . .	32
2.4	Manufacturability . . . . .	33
2.5	Conclusion . . . . .	35

<b>3 Conclusion</b>	<b>37</b>
<b>A Impingement jet cooling</b>	<b>38</b>
A.1 Impingement Jet Cooling . . . . .	38
A.1.1 The Single Impingement Jet . . . . .	38
A.1.2 Multi-jet impingement . . . . .	40
<b>B Turbulator</b>	<b>41</b>
B.1 Turbulator . . . . .	41
B.1.1 Pin-Fin Turbulator . . . . .	41
B.1.2 Dimples . . . . .	43
B.1.3 V-rib Turbulator . . . . .	43
B.1.4 Conclusion . . . . .	46
<b>C Impingement Jet array on Flat Smooth Target (Baseline)</b>	<b>47</b>
C.1 Experience . . . . .	47
C.1.1 The Particle Image Velocimetry . . . . .	47
C.1.2 Experience Setup . . . . .	48
C.2 Numerical Modelling . . . . .	48
C.3 Results . . . . .	50
C.3.1 Flow Field . . . . .	50
C.3.2 Heat transfer . . . . .	52
C.4 Validation . . . . .	53
C.5 Conclusion . . . . .	54

# List of Figures

1.1	Schematic of a gas turbine [16] . . . . .	2
1.2	Brayton cycle . . . . .	2
1.4	Oktoberfest traditions . . . . .	7
1.5	Work office . . . . .	7
1.6	The award of the doctoral degree in Turbine department . . . . .	8
1.7	Christmas Market in Göttingen . . . . .	9
2.1	The ArcConic on the hole plate . . . . .	14
2.2	Unstructure grid of the multi-impingement jet configuration with the ArcConic . . . . .	14
2.3	Spanwise-averaged Nusselt number on the fine grid with the CGI error bars, ArcConics . . . . .	16
2.4	Validation of a V-rib on the hole plate . . . . .	18
2.5	Area averaged heat transfer ( $Nu/Nu_0$ ) and friction factor ( $f/f_0)^{1/3}$ . . . . .	19
2.6	Schematic of the flow field for jets #6-8, Smooth and ArcConic . . . . .	20
2.7	Velocity magnitude in the center plan . . . . .	22
2.8	Effective individual jet Reynolds number fraction normalized by $Re_{mean} = 10,000$ . . . . .	23
2.9	Effective jet mass flow distribution, $Re_{mean} = 10,000$ . . . . .	23
2.10	Local Nusselt number distribution on the target plate, the red dots indicate geometric jet centers, $Nu_0 = 45$ . . . . .	25
2.11	Spanwise averaged Nusselt number normalized by $Nu_0$ , $Nu_0 = 45$ . . . . .	26

2.12 Effect of Reynolds number, nornalized spanwise averaged Nusselt number by $Re^{\frac{2}{3}}$	27
2.13 Effect of the rib position $x/D$ on $Nu/Nu_0$ and $C_d/C_{d,0}$ ; $Nu_0 = 45$ , $C_{d,0} = 0.62$ , $Re = 10,000$	28
2.14 Effect of rib height $e_1/D$ on $Nu/Nu_0$ and $C_d/C_{d,0}$ ; $Nu_0 = 45$ , $C_{d,0} = 0.62$ , $Re = 10,000$	29
2.15 Effect of rib length $B_1/D$ on $Nu/Nu_0$ and $C_d/C_{d,0}$ ; $Nu_0 = 45$ , $C_{d,0} = 0.62$ , $Re = 10,000$	30
2.16 Effect of rib Sharpe $e_2/D$ on $Nu/Nu_0$ and $C_d/C_{d,0}$ ; $Nu_0 = 45$ , $C_{d,0} = 0.62$ , $Re = 10,000$	31
2.17 Effect of separation distance $H/D$ on $Nu/Nu_0$ and $C_d/C_{d,0}$ ; normalized by the according values for the smooth configuration	32
A.1 Impingement jet flow-structure [7]	39
B.1 Structure flow in pin-fin channel	42
B.2 Structure flow in dimples channel	44
B.3 V-Ribs in flow channel	45
C.1 Experimental Setup $\frac{2D}{2C} - PIV$ in $XZ - plane$ orientation showing 1 light-sheet optic, 2 square cross-section channel, 3 SC莫斯相机, 4 laser head, 5 settling chamber, 6 orifice metering section, 7 blower, 8 2-axes traversing unit [58]	49
C.2 Mean velocity distribution in the mid-plane ( $y = 0$ [58])	50
C.3 Vorticity distribution in the direction of crossflow [58]	51
C.4 Nusselt number distribution on the heated plate, the red dots indicate geometric jet centers	52
C.5 Validation Smooth DLR with Tabassum data	54

# List of Tables

2.1	Grid parameters for the ArcConic configuration . . . . .	15
2.2	Validation of smooth configuartion . . . . .	17

# **Nomenclature**

entryA You may include nomenclature here.

$B_{1\&2}$	Axes of the ellipse	m
$C_d$	Discharge coefficient: $\frac{\dot{m}}{(N \cdot \frac{D^2}{4} \cdot \pi) \cdot \sqrt{2 \cdot \Delta \bar{P} \cdot \rho}}$	-
$D$	Jet diameter (0.0152 m)	m
$e_{1\&2}$	height of the rib	m
$f$	Friction factor: $\frac{\Delta \bar{P}}{2 \rho u_{\text{inlet}}^2} \frac{D}{L}$	-
$H$	Separation distance	m
$k$	Thermal conductivity	W/mK
$L$	Length	m
$Nu$	Nusselt number: $\frac{q_{\text{wall}} D}{k_t (T_{\text{wall}} - T_{t\text{jet}})}$	-
$p$	Pitch	m
$P$	Pressure	Pa
$\Delta \bar{P}$	Pressure difference: $\overline{P}_{\text{inlet}} - \overline{P}_{\text{outlet}}$	Pa
$Pr$	Prandtl number	-
$q_w$	Specific wall heat flux	W/m <sup>2</sup>
$Re$	Reynolds number: $\frac{u_{\text{jet}} D}{\nu_{\text{jet}}}$	-
$T$	Temperature	K
$u, v, w$	Velocity components	m/s
$u^*$	Velocity Magnitude: $\frac{v}{v_j}$	-
$x, y, z$	Coordinates	m
$y_1^+$	Near-wall grid size (wall-normal)	-
$W$	Width	m
$\rho$	Density	kg/m <sup>-3</sup>
$\nu$	Kinematic viscosity	m <sup>2</sup> /s
$\vec{\omega}$	Vorticity: $\nabla \times \vec{v} = \left( \begin{array}{c} \frac{\partial v_z}{\partial y} - \frac{\partial v_y}{\partial z} \\ \frac{\partial v_x}{\partial z} - \frac{\partial v_z}{\partial x} \\ \frac{\partial v_y}{\partial x} - \frac{\partial v_x}{\partial y} \end{array} \right)$	s <sup>-1</sup>

---

$B_1$	shape of the rib	mm
$e_1$	height of the rib	mm
$e_2$	shape of the rib	mm
$x$	Position of the rib	mm

# **DLR Presentation**

DLR is the abbreviation for Deutsches Zentrum für Luft-und Raumfahrt that can be translated as the German Aerospace center. The German Aerospace center has been created in 1969 under the name the Deutsche Forschungs- und Versuchsanstalt für Luft- und Raumfahrt (DFVLR, German Test and Research Institute for Aviation and Space Flight) after the merger of several Research center in Germany such as the Aerodynamisch Versuchsanstalt (AVA, Aerodynamic Experimental Station) created in 1907 by Ludwig Prandtl in Göttingen that is considered as to the birthplace of modern aerodynamics), the Deutsche Versuchsanstalt für Luftfahrt (DVL, German laboratory for aviation, created in 1912 in Berlin) and the Deutsche Forschungsanstalt für Luftfahrt (DFL, German Research institute for aviation, created in 1936). In 1997, the name has been changed to DLR. The headquarters of DLR are situated in Cologne and count 20 locations composed to 48 institutes through Germany as illustrated in Figure XXX and has offices in Paris, Brussels, Tokyo and Washington. The DLR has different type partner: Research center such as the European Space Agency (ESA) and the European Organisation for the Exploitation of Meteorological Satellites (EUMETSAT); industries such as Rolls Royce, Siemens and universities. Its principal clients are the German Federal Government as the German Federal Ministry for Economic Affairs and Energy, together with federal state authorities, but it also services educational institutions, foundations and associations, as well as the European Commission.

The DLR Göttingen where my internship took place is the oldest center of the DLR group and the world's first state aviation research institution. It has nearly 500

specialists working on different purposes as on the aircraft, spaceships and the high speed train of the future. This center is separated in three institutes:

- The aeroelasticity institute
- The aerodynamics and fluid mechanics institute
- The propulsion technology institute

In these premises, There are more than 20 wind tunnels, a catapult for research into high-speed trains, an air traffic simulation facilities, wind tunnels in the European DNW foundation (German-Dutch Wind Tunnels), mobile rotor test stands and test stands for material and noise tests. Also, there are the DLR School lab, DLR systems Engineering, DLR Technology Marketing, and DLR Central Archive. My internship took place in the institute of propulsion technology in the turbine department called AT-TUR which works with different industries such as Siemens in order to improve gas turbine. Also, the turbine department makes researches about the heat transfer and cooling effectiveness.

# Chapter 1

## Introduction

### 1.1 Turbine Cooling

Gas Turbine plays a vital role in the today's industrialized society, indeed it is used for aircraft propulsion and power generation. In addition, the demand for power increases considerably due to a demographic explosion, and an economic growth, digitalization and development of mobility.

Gas Turbine is a rotary machine in which air is compressed by a compressor, and delivered into the combustor as illustrated in Figure 1.1. The fuel is injected into the combustor and mixed with the hot compressed air, and it is burned at a constant pressure which characterizes the combustion process. After the combustion, the hot mixture is delivered into the turbine. The turbine extracts kinetic energy from the gas thanks to the turbine blades. Thus, a part of the created energy is used to turn the compressor because the turbine is mechanically coupled to the compressor by a centrally rotating shaft, and the rest can be used for different purposes such as generators for power generation.

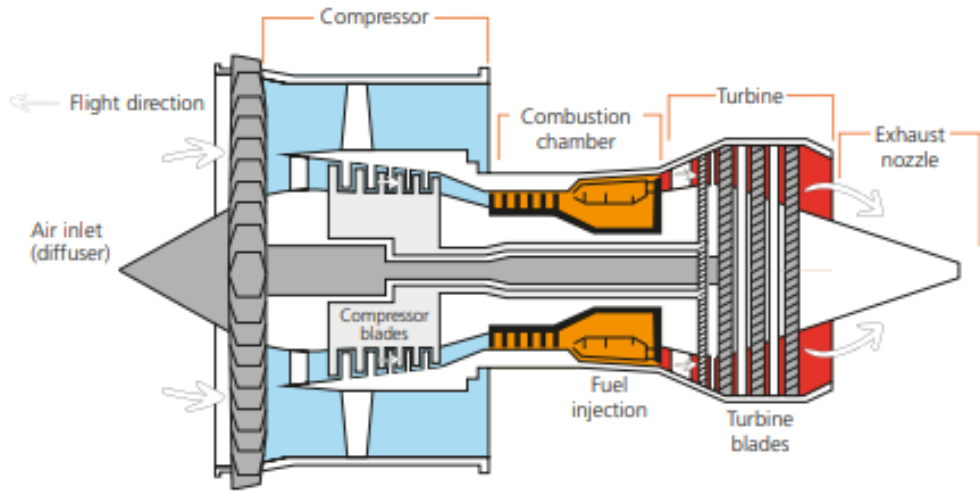


Figure 1.1: Schematic of a gas turbine [16]

Currently, the Brayton cycle describes the working of a gas turbine [20]. From the compressor, the inlet air is compressed by the compressor, it happens an isentropic combustion. Then, there is a heat addition at constant pressure that illustrates the combustion. After that, there is an isentropic expansion which meaning the pressure decreases into the turbine. Finally, there is a heat rejection at constant pressure in order to close the cycle.

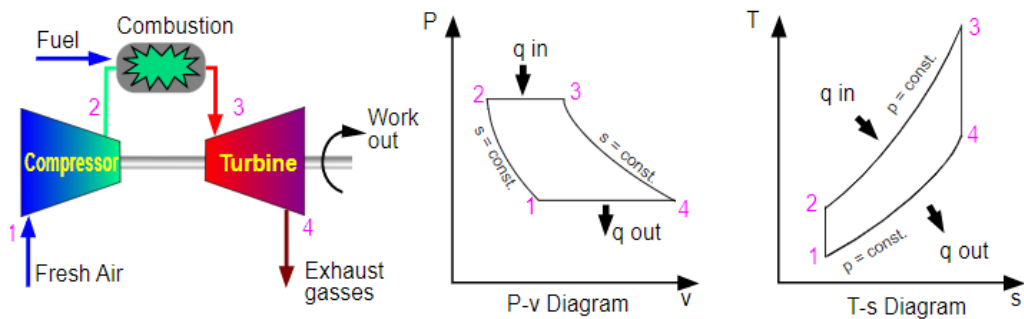
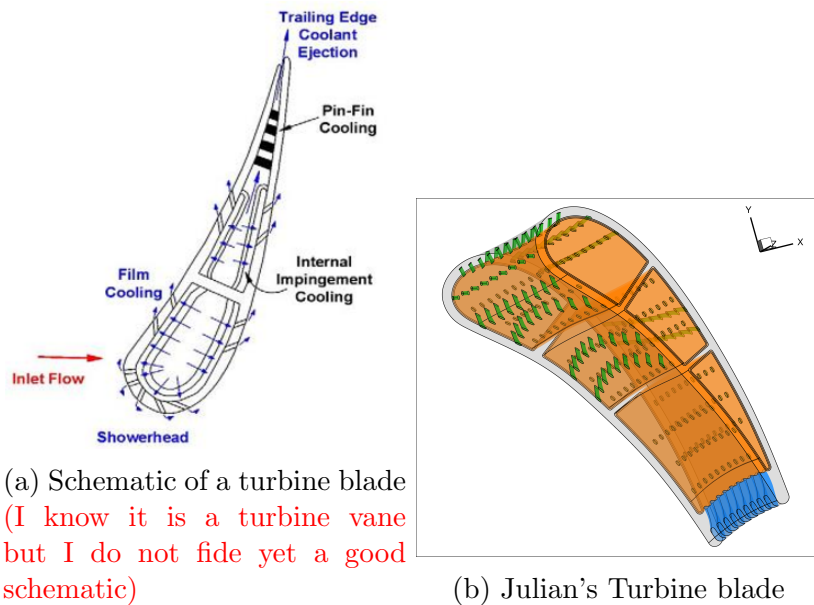


Figure 1.2: Brayton cycle

The overall efficiency of the gas turbine depends on the exit temperature after the

chamber combustion. During several years, Gas Turbine is improved in order to enhance reliability, both thermal and economical efficiency and the reduction of critical emissions. For optimal efficiency, the turbine inlet temperature needs to be higher from the melting point that damaged the components of the turbine.

The temperature entering the turbine can be over 200 °C [54] from the melting point of the material of the turbine blades. In addition to using a material with better thermal properties, it needs to use cooling methods in order to cool blades, and so limit the damage to the turbine blades.



As shown in the figure 1.2, the blade used internal and external cooling as film protection of coolant air around the surface of the blade named Film cooling. For the internal cooling, a coolant passes to channel cooling, jet impingement or Pin-fin cooling system. The blade is hollow, so cooling air can pass through the blade internally characterised the channel cooling illustrated in orange in Figure 1.2. Impingement cooling is used near the leading edge of the blade and near the mid-chord of the blade where the temperature is higher because it offers a high cooling efficiency. This method consists to hitting the surface of the blade with high velocity air. Thus, it removes heat from the blade wall. Due to manufacturing constraints in the narrow

trailing edge of the blade, Pin-Fin cooling is used to improve the heat transfer. This is an array of pin-fins and the flow around the pins forms just upstream of the base of the pin vortex which enhances the heat transfer. After impinging on the walls of the airfoil, the coolant exits the blade through multiple small holes represented by green holes in Figure 1.2. Additionally, the coolant travelling through the pin-fin array is ejected from the trailing edge of the airfoil illustrated in blue the trailing edge cooling shots. But the pressurized cooling air is taken out of the compressor that reduced the overall efficiency of the gas turbine because 3% to 5% [7] of the compressor air is not used into the combustion and does not contribute into the power generation. So, air supply for cooling has been minimized in order to enhance the efficiency of the gas turbine. The current work is focus only on Impingement Jet cooling because the multi-jet configuration generated complex jet interactions presented in **Appendix A** which affects the cooling efficiency.

## 1.2 Aim of the work

The courses of my internship are divided into three phases. Firstly, I studied an array of impingement jets on a flat surface in order to validate my results with Tabassum data [58] which explained in **Appendix C**. Secondly, I made a comparative study for the impingement configuration with Vrib turbulators on the impingement plate between my results and Chen data [15] presented in **2.2.2**. Finally, I studied ArcConic turbulator on numerical work on a generic impingement cooling system presented in **2.3**. Then, I participated in writing on ASME paper 2023 with InnoCool project presented in Chapter 2. The work of this report is summarized behind following:

- Literature review with focus on the smooth case and V-Rib case
- Problem statement
- Tools selection and Method define
- Simulations
- Data analysis

- Selection of turbulator to be investigated into the ASME paper
- Write results in ASME paper

## 1.3 The human aspect during my internship

### 1.3.1 Team presentation

In this part, I will present all people which I worked with them.

First, we have Frank Kocian, the head of the turbine department. He has a global view on all project in the turbine department, and he follows the progress of all projects.

During my internship, I was working on InnoCool project. This project consists to create a new turbulator using the crossflow in order to improve the cooling efficient in an impingement configuration; and write a scientific paper in order to explain our work. The team of the InnoCool project is composed to: Robin G. Brakmann; Nina Brose and Francisco Carvalho as illustrated in Figure XXX.

Robin G. Brakmann is the deputy to Frank; and is the team leader of different project. His function allows to manage the different projects, spread the stains with other team members, and direct the projects. He is the principal element that generating team spirit in order to create a communication between the team members. But, in case of Frank absence, he replaces him. Moreover, he is my tutor during my internship. His function is to accompany me during the internship with the help of Nina Brose.

Then, we have Francisco Carvalho is considered as the functionnal respondable in InnoCol project. Indeed, he conducts the overall operations required for the preliminary study making different researches and he has the responsibility to leading the editors for the ASME paper.

In opposition to Nina Brose, she only managed the technical aspects of the project. She implements the development of the new product inspired to the V-Rib turbulator. She creates the geometry of the new configuration in CATIA presenting in Figure 2.1.

Moreover, she ran CFD simulations for analyze the phenomena in this configuration. During my internship, Nina trained me to use the different software tools for running simulations.

My work consists to run CFD simulations for different cases under different flow conditions. I created a data base for the impingement configuration with ArcConic turbulators on the hole plate. Thus, I saved my colleagues a lot of time and I enabled the company to improve productivity and efficiency. Indeed, during my internship, I have done XXX hours of simulations. Moreover, I participated in writing of ASME paper 2023.

In the end of the project, InnoCool project will make experience study with the new turbulator. Also, the configuration will give to the other team project managed by Mr Brakamnn, Robin Schöffler and Julian Lüken, in order to create in three-dimensionnal a turbine blade with the ArcConic turbulators on the hole plate for impingement cooling.

### **1.3.2 The memories during my internship**

During the end of September, I discovered the Oktoberfest presenting by my colleagues during a lunchtime and celebrating with the Erasmus Group. The Oktoberfest is a German tradition celebrated with beer. It consists to drink a Mass that is 1L of beer as shown in Figure 1.4 (a) and to wear the traditional Bavarian costume (=but it is not an obligation). For men, this means wearing a Lederhose, a traditional short panty with a bridge, and for girls the famous Dirndl dress. Moreover, the Oktoberfest is a place for funfair as shown in Figure 1.4 (b).



(a) Mass

(b) Oktoberfest funfair Hannover

Figure 1.4: Oktoberfest traditions

During my internship, I worked in the same office to Julian Lüken in which we had a tradition established by Mr. Brakmann. This tradition consists to stick a hedgehog meme on the wall every time we success something in our work as illustrated in Figure 1.5. Julian Lüken was a computer science student that worked for DLR in order to write some code which allows to create the turbine blade geometry. In addition, he had written his thesis for his last year of master about his works in DLR. He helped me for some parts of my work as writing in Latex or using python in order to create graphs for the ASME paper and my report. His referent was Robin Schöffler.



(a) Hedgehog Tradition

(b) His thesis

Figure 1.5: Work office

The November 25, Turbine Department celebrated the award of the doctoral degree for Anna Petersen, Christian Zurmühlen and Clemens Gruntwitz. Due to the pandemic, they did not have the occasion to celebrate it. For this celebration, some colleagues designed the mortarboard. Each mortarboard have been designed to fit the person with symbols illustrating those years of thesis as shown in Figure 1.6 (b). The tradition during the award of the doctoral degree in Göttingen consists to march from the DLR to the Gänselfiesel that is the symbolic statue of Göttingen located in front of the old city hall. During this march, the AT-TUR doctoral students are seated in a car as shown in Figure 1.6 (a) and weared their mortarboard. Arriving to the Gänselfiesel, the doctoral student must place a bouquet of flowers on top of the fountain and kiss the cheeks of the statue.

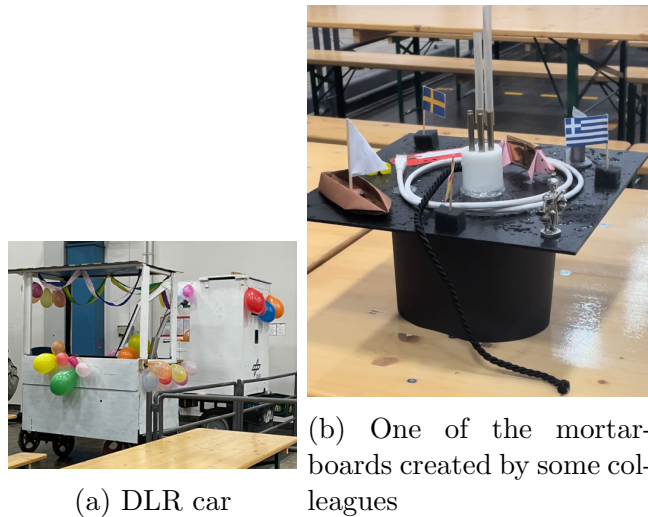


Figure 1.6: The award of the doctoral degree in Turbine department

During the Christmas period, some colleagues organized some after-work in the Christmas Market in Göttingen where they presented me some German specialities as mulled wine, roasted almonds, Gingerbread and Schmalzkuchen. I also participated in the Christmas meal with all people in Turbine department.



Figure 1.7: Christmas Market in Göttingen

# Chapter 2

## Result: ASME paper

### 2.1 Introduction

The turbine inlet temperature in modern gas turbines increasingly exceeds material limits and cooling is required to avoid component failure. Jet impingement arrangements offer high cooling efficiency and are therefore frequently used. However, the physics of multi-jet configurations is associated with complex jet interactions. Reviews of the underlying physical phenomena and recent developments on heat transfer enhancement are compiled in e.g. [45, 77, 68, 18].

The literature discusses numerous approaches for heat transfer enhancement. Micro pin fins on the target surface [30, 13, 6, 8, 61] or on the hole plate [17] increase surface area and turbulence. The result is a thinner thermal boundary layer and higher heat transfer rate. Similarly, dimples on the target plate generate swirling flows and turbulence with comparatively low pressure losses [34, 32]. Inclined impingement jets [24], swirling jet nozzles [74, 31] and oscillating jets [71, 37] provide a more homogeneous heat transfer distribution over the target plate. Combining target and hole plate micro-structures opens up further possibilities such as concentrical impingement zones [33] also integrate [38] into this paragraph. In addition, V-ribs can be placed on the target plate to protect the impingement jet from the cross-flow [14].

In the presence of a V-rib, the cross-flow is split into two streams, each following the rib contour and returning to the centerline where it reattaches to the target plate [29]. The cross-flow is redirected away from the jet, reducing loss of jet kinetic energy and increasing heat transfer. This protection leads to a particular benefit in the stagnation region, with the Nusselt number reaching up to four times the baseline value [49] at  $H/D = 2$  and  $Re_{channel} = 67,000$ . An improvement in averaged heat transfer is further reported [75, 10, 3] for inline row, inline array and staggered array multi-jet configurations. Apart from the stagnation point improvement, [75] documents an averaged  $Nu$  increase of up to 42% with  $H/D = 6$  and  $Re_{jet} = 3,000$ . Ranges between 15% and 42% depending on the cross-flow arrangement. An increased averaged heat transfer is also reported for staggered and inline impingement cooling arrangements [10, 3]. However, [49, 3] report on a heat transfer drop in the upstream jet region in comparison to a smooth channel, possibly as a result of the cross-flow entrainment caused by the V-ribs. It is mostly in the downstream jets, where the cross-flow builds up, that the V-rib shows potential. Additionally and most critical, V-ribs generate additional pressure losses due to the cross-flow blockage and the induced secondary flow structures. Rhee et al. [53] report a pressure loss increase of up to 20% for 90° V-ribs due to the secondary flow structures generated in the channel.

In essence, cross-flow is an undesirable factor that can be downplayed with certain micro-structures such as V-ribs, at the expense of pressure losses. But is it possible to turn cross-flow into an asset, instead of trying to minimize its negative effects?

Combining target plate V-ribs with inverted V-ribs on the hole plate can intensify the momentum of the impingement jet. The bottom rib shields the impingement jet from the cross-flow and redirects it towards the side walls and upwards to the hole plate. The deflected cross-flow meets the hole plate V-rib and is guided to the impingement hole, increasing the jet  $Re$  number and massflow. This results in a significantly reduced jet deflection [14] and the effect increases with the cross-flow. Thinking in terms of small scale manufacturability, it is less challenging to achieve a precise rib-to-jet placement on the hole plate than on the target plate. With this motivation, a configuration is selected with only hole plate V-ribs. While the stagnation region is no longer protected, the jet momentum is still increased through the redirected cross-

flow, leading to an averaged  $Nu$  number increase of 6% at  $H/D = 4$  and  $Re_{channel} = 35,000$  Look at comment in pdf-Seite 116. It seems like the hole plate ribs are the biggest generators of pressure losses. The benefit is negligible in the upstream jets and grows further downstream with increasing cross-flow [14]. The stagnation  $Nu$  number increases and moves slightly upstream as a result of the smaller jet deflection. Furthermore, in the absence of target plate V-ribs, the cross-flow in the upstream region is unobstructed and there is no heat transfer decrease compared to a smooth channel configuration. Wang et al. [62, 63, 64] also take advantage of the cross-flow to increase heat transfer by placing a vortex generator on the hole plate, upstream of a single jet in cross-flow. The generated vortex pair pulls the cross-flow away from the hole plate, increasing its boundary layer thickness and decreasing its axial momentum. Jet penetration in the cross-flow is thus improved. In addition, the cross-flow between the vortex pair itself interacts with the jet to increase its momentum. This results in a higher stagnation region heat transfer with a slight shift in the upstream direction[62] figure 6. The opening angle  $\lambda$  is varied between  $30^\circ - 90^\circ$  and the height  $e$  is varied between  $0.5D$  and  $1.5D$ . At  $Re_{channel} = 40,000$  and  $Re_{jet} = 15,000$ , The average  $Nu$  number increases up to 37% with an opening angle of  $90^\circ$  and a rib height of  $e = 1.5D$ . Accordingly, both the pressure drop of the jet and cross-flow increase by up to 24% and 49%[63] table 2. In short, cross-flow can be used to improve heat transfer. The magnitude of this improvement and of the associated pressure losses will depend on the turbulator.

With this background, the current work introduces the ArcConic as an iteration of the V-rib. This U-shaped turbulator is installed downstream of the jet hole. The arrangement redirects the cross-flow into the jet, increasing its effective Reynolds number and thus the Nusselt number on the target plate. This turbulator does not modify the target plate, so it can be combined with other surface modifications. The numerical work focuses on a generic impingement cooling system and on the simulation of a large number of configurations in a cost effective manner. The presented geometry is of interest for designers of impingement cooling systems under high cross-flow condition.

## 2.2 Numerical Setup

### 2.2.1 Geometry

The generic jet impingement cooling system is shown in Figure 2.2. The arrangement consists of nine inline circular jets in a row with a jet pitch of  $p/D = 5$ . Each jet has a diameter of  $D = 0.0152$  m and is impinging on a heated target flat plate. The square cross-section of the channel has an edge size of  $H/D = W/D = 5$  and a nozzle length of  $3D$ . In this setup a cross-flow is self-induced by the spent cooling air before leaving the domain through the outlet. The numerical setup and the according experimental apparatus for a smooth configuration are described by Tabassum et al. [57] and Schroll et al. [schroll2022], for this study turbulators were added to the hole plate. The ArcConic shown in Fig. 2.1 has an U-shape with the apex pointing in the direction of the outlet. The apex is placed in a distance  $x$  downstream of the jet center. The ArcConic is defined by an ellipse with the major axis  $B_1$  and the minor axis  $B_2$ . The height and shape of the rib are defined by a cubic Bézier spline with two points ( $e_1$  and  $e_2$ ) with a tangent tension  $s = 1$ . For the following investigation the minor axis  $B_2 = 13.2D$  and the rib width of  $1/2D$  are kept constant. The remaining parameters assume the following initial values designated with **(R)**:  $B_1 = 13.2D$ ,  $x = 0.8D$ ,  $e_1 = 1D$ ,  $e_2 = 0.5D$  and  $x = 0.8D$ . This initial geometry results in a 20% area increase of the hole plate.

### 2.2.2 Steady-RANS Simulations

The working fluid is considered to be an ideal gas ( $R = 287$  J/kgK,  $\gamma = 1.4$  and  $Pr = 0.71$ ). Except for the heated target plate, all walls are treated as adiabatic. The inlet boundary conditions are set with a total temperature of  $T_0 = 298.2$  K, a total pressure of  $P_0 = 102,099$  Pa, a turbulence intensity of 1% and the turbulent length scale of 0.003 m. The mass flow rate at the outlet is set to  $\dot{m} = 0.019982$  kg/s for an average jet Reynolds number of  $Re = 10,000$ . On the heated target plate an isoflux boundary condition with  $q_w = 5,000$  W/m<sup>2</sup> is applied. The RANS simulations are performed using the density-based compressible finite volume solver TRACE [28]. Turbulence is handled with the Menter k- $\omega$  SST 2003 model [47]. The standard

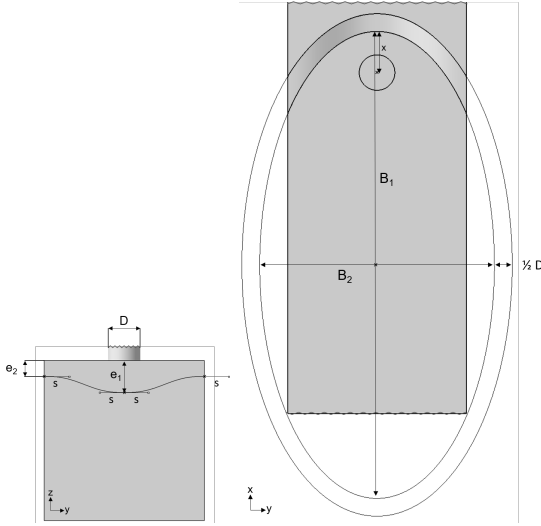


Figure 2.1: The ArcConic on the hole plate

SST model is modified by including the Langtry and Menter two-equation transition model [40] and the production limiter by Kato-Launder [36]. CENTAUR [12] is used to generate the unstructured grid with tetrahedral elements shown in Figure 2.2. The grid structure corresponds to the grids used in our previous study [schroll2022, 57].

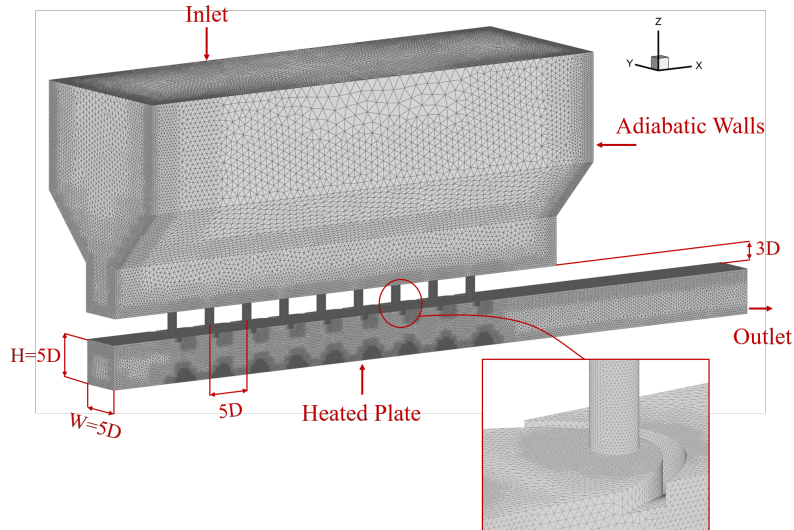


Figure 2.2: Unstructure grid of the multi-impingement jet configuration with the ArcConic

### 2.2.3 Convergence and Grid Quality

The discretization error is quantified with the Grid Convergence Index (GCI) [11]. This method is a standardized method to analyze the dependence of the numerical solution on spatial discretization. By considering the absolute errors of the variables of interest for different grids and levels of refinement the GCI error is calculated. An initial grid is coarsened twice in every direction, including the cells at the wall. The parameters considered for the three meshes are listed in Tab. 2.1.

Table 2.1: Grid parameters for the ArcConic configuration

Grid	Mean near-wall dimensionless distance ( $y_1^+$ )	No. of prism layers	Total no. of elements	Area-averaged height Nusselt number
Fine	0.32	20	20646253	47.5
Medium	0.44	18	10343181	46.72
Coarse	0.60	17	5738604	45.70

For the GCI analysis, the Nusselt number on the heated target plate is considered. The spanwise-averaged  $Nu$  numbers and the resulting error bars obtained through the GCI of the fine grid are depicted in Figure 2.3. The highest errors occur in the peaks of the  $Nu$  number, corresponding to the jet stagnation points. These regions tend to have excessive turbulence production and are problematic for two-equation turbulence models [77]. Larger errors can also be seen where the wall jets collide ( $Nu$  number minima), a region also characterized by higher turbulence production. The median error of the  $Nu$  number is  $\approx 3\%$  and reaches a maximum of 15-20% at the peaks. The relatively high discretization errors reflect the unsteady nature of the flow. The grid is considered sufficiently accurate for the scope of the current study, and further simulations are performed using the fine grid. A mass flow rate fluctuation below  $10^{-7}$  is set as convergence criterion.

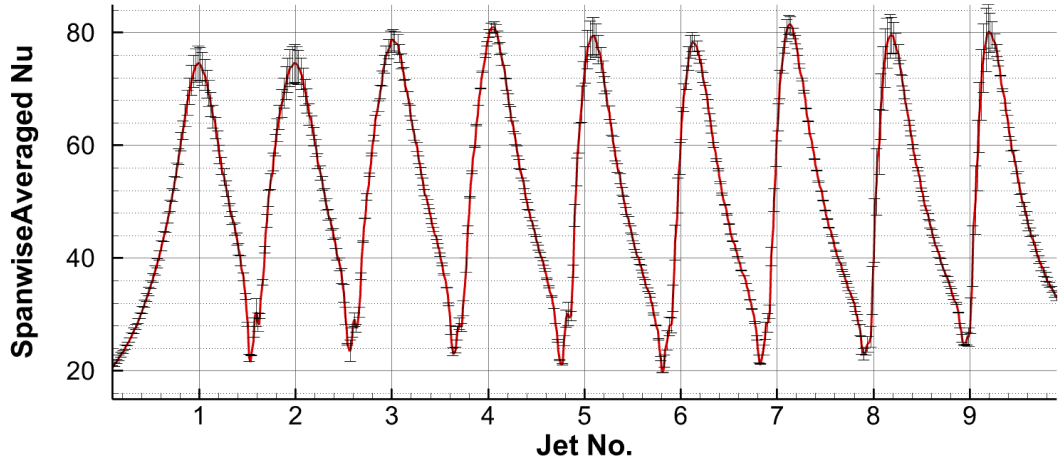


Figure 2.3: Spanwise-averaged Nusselt number on the fine grid with the CGI error bars, ArcConics

#### 2.2.4 Validation

The literature provides various  $Nu$  number correlations for impingement jet configurations with a smooth hole plate. Table 2.2 lists the predicted Nusselt number values from this study against such correlations for a similar configuration. The area-averaged Nusselt number for an array of impingement jets is described by the correlations [45, 27, 48]. The correlation [70, 51] for the stagnation  $Nu$  number of a single jet is further compared against jet #3. Due to the relatively small influence of the cross-flow and the adjacent jets on both sides, it resembles a single jet. Despite minor differences, a good agreement is achieved. The validation of the smooth configuration is discussed in greater detail in Tabassum et al. [57].

Table 2.2: Validation of smooth configuartion

Correlation parameter	Calculated from literature	Current study
[45] $\overline{Nu}$ Array	44	45 (+2.7%)
[27] $\overline{Nu}$ Array	48	45 (-5.3%)
[48] $\overline{Nu}$ Array	44	45 (+2.7%)
[70] $Nu_s$ Jet #3	113	107 (-5.3%)
[51] $Nu_s$ Jet #3	123	107 (-12.7%)

For validation of the ArcConic geometry, V-ribs [14] are used as reference. These V-ribs are positioned in the same way as the ArcConic and guide the flow in a similar fashion. The ribs have a square cross-section ( $w/D = e/D = 0.5$ ) and an opening angle of  $90^\circ$ . The apex of the V-rib is positioned  $1.3D$  apart from the jet center. Please note that Chen et al. [14] uses a slightly different geometrical setup, CFD solver and grid. The experiments are performed using the thermo-chromic liquid crystals (TLC) methodology. The spanwise Nusselt numbers shown in Fig. 2.4 are normalized with the according smooth baseline geometries. The jet deflection and the augmentation of the Nusselt number is predicted correctly in TRACE. Hence, the quality of the CFD analysis is deemed sufficient for this study.

## 2.3 Results

### 2.3.1 Parameter variation

Over 100 variations of the ArcConic have been simulated. The results of the area averaged  $Nu$  number and friction factor augmentations are shown in Fig. 2.5. Additionally the increase in Nusselt number and friction factor with the Reynolds number of a smooth configuration is depicted in two solid lines. The values are normalized with the according smooth baseline case (index 0). An ArcConic configuration situated left of the solid lines performs better than if the additional pressure loss would be used to increase the Reynolds number on a smooth configuration.

In the next section various geometric effects are discussed. We show the Nusselt

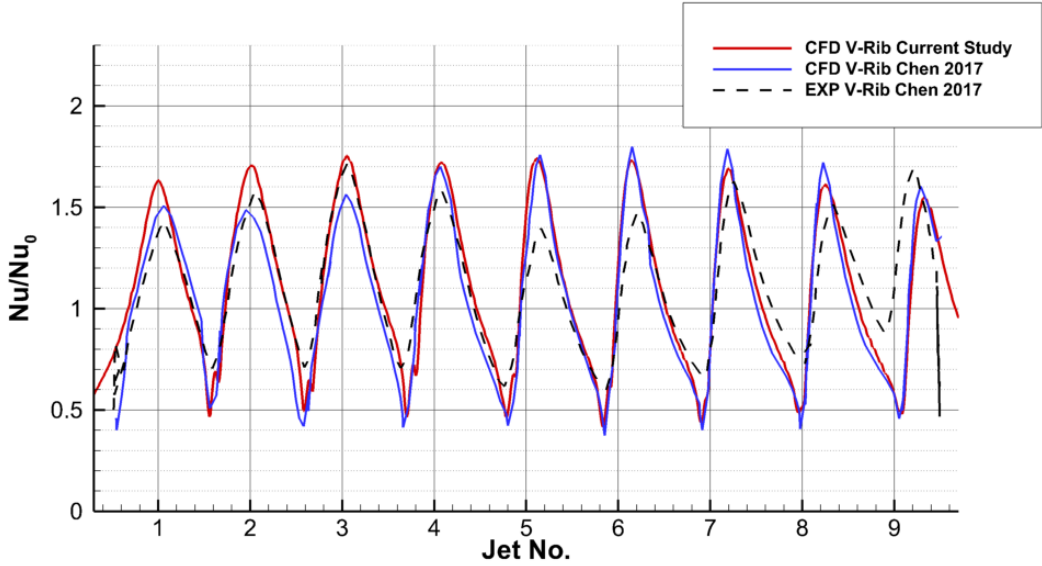


Figure 2.4: Validation of a V-rib on the hole plate

number enhancement,  $Nu/Nu_0$ , in orange and the evolution of the pressure loss ratio  $C_d/C_{d0}$  in blue, relative to the smooth hole plate (index 0). An increase in both ratios is positive - meaning increased heat transfer and decreased pressure loss. The most interesting configurations are marked with special symbols and are analysed in the following sections in greater detail. These include the initial ArcConic configuration in red, mentioned in Sec. 2.2.1 and marked with an **R**, as well as points with particularly high heat transfer augmentation (**V** & **B**), low pressure penalty (**M**), especially high pressure penalty (**N**) and one option with a rib upstream of the hole (**L**). The parameters for these configurations are listed in Fig. 2.5.

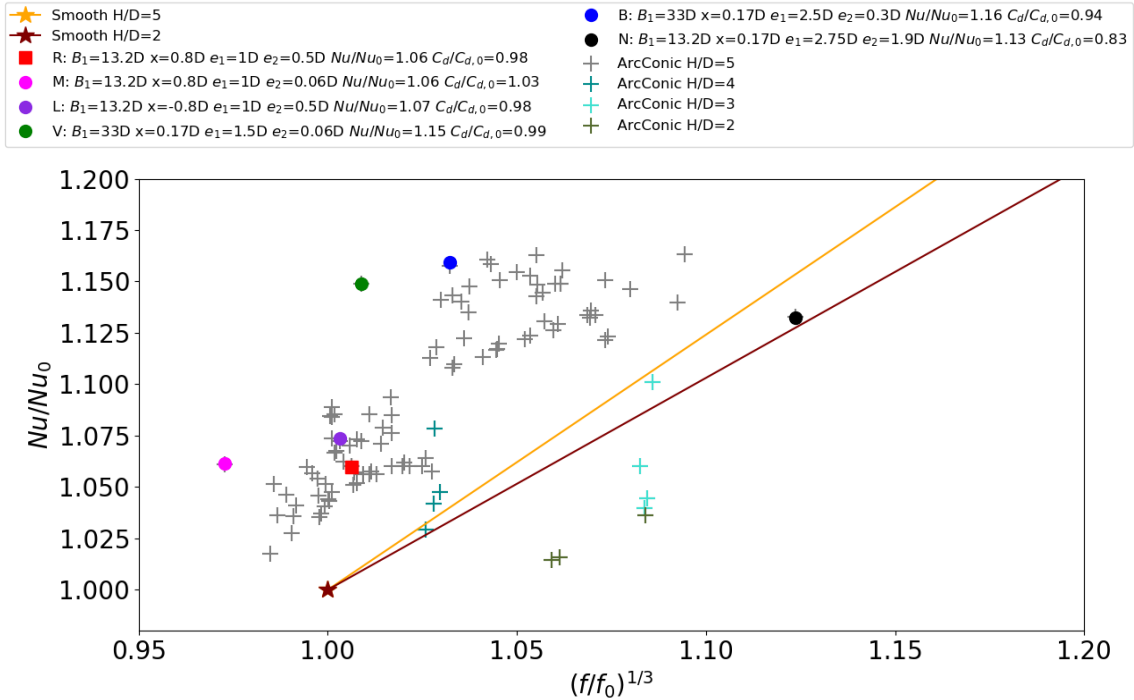


Figure 2.5: Area averaged heat transfer ( $Nu/Nu_0$ ) and friction factor ( $f/f_0)^{1/3}$

### 2.3.2 Flow Field

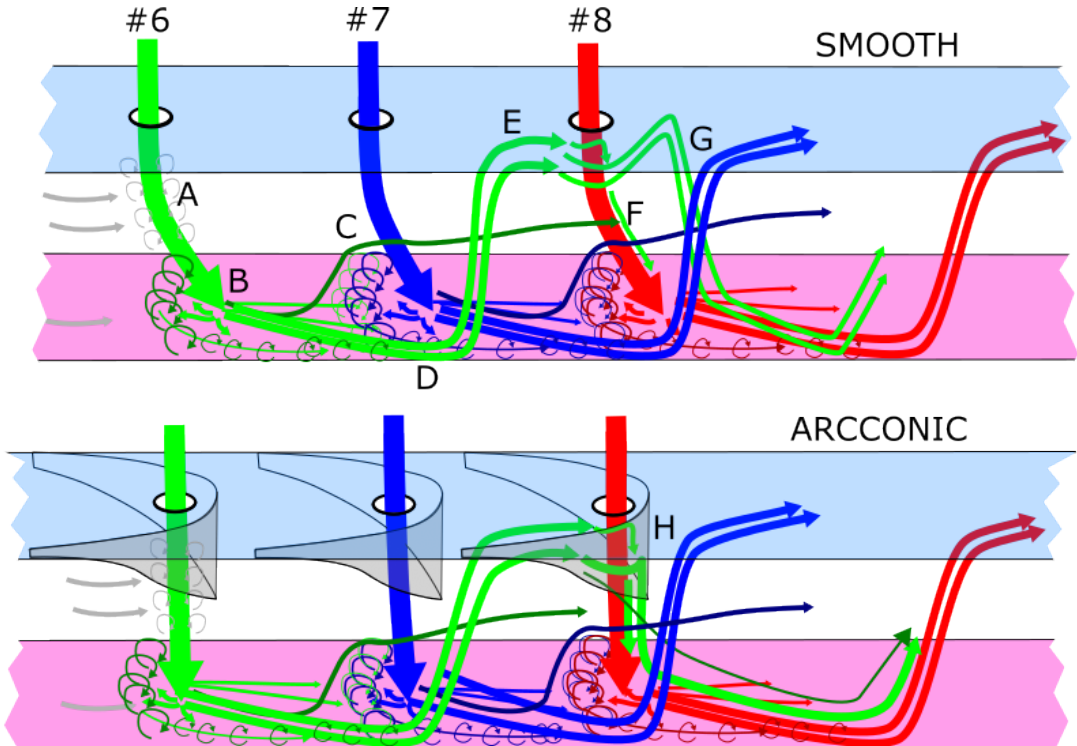


Figure 2.6: Schematic of the flow field for jets #6-8, Smooth and ArcConic

The complex flow field of an impingement jet array in maximum cross-flow is shown schematically in Figure 2.6. The jets #6, #7 and #8 already have a certain amount of self-induced cross-flow. The depicted flow phenomena have a repeating pattern and are self-similar. The center plane velocity magnitude for the smooth and selected ArcConic configurations is presented in Fig. 2.7. The jets emerge from the impingement hole as a free jet (A Fig. 2.6) and directly interact with the surrounding fluid which is entrained into the jet. In the stagnation zone (B Fig. 2.6), the jet encounters an adverse pressure gradient and the velocity is decreased to zero. After impingement, the pressure field accelerates the flow in the radial direction forming the wall jets. The wall jets of adjacent impingement jets collide head to head (C Fig. 2.6) forming a secondary stagnation zone. The resulting fountain flow is rolled up to a vortex upstream of the stagnation point. The fluid is displaced by the adjacent jet towards

the side walls (**D** Fig. 2.6). The fluid follows the walls and reaches the hole plate between the next and the after next jet (**E** Fig. 2.6). Some of this fluid re-enters the impingement jet (**F** Fig. 2.6), the rest joins the cross-flow and recirculates in an helical movement towards the outlet (**G** Fig. 2.6). The cross-flow deflects the jet and its path towards the target plate is extended (e.g. jet #7, smooth, Fig. 2.7). This increases the shear effects and has a negative effect on the heat transfer. The increasing amount of self-induced cross-flow increases the channel velocity and decreases statistic pressure in the channel. This effect draws more air from the plenum in the downstream jets increasing their individual jet Reynolds number as shown in Figure 2.8. The graph shows the individual jet Reynolds number distribution in the jet hole, normalized by the average Reynolds number of 10,000. Only the very large rib (**N**) deviates significantly from the smooth distribution. The cross-flow velocity is increased by the rib and more air is drawn from the plenum.

The ArcConic configuration guides more cross-flow air into the jet (**H** Fig. 2.6) and increases the effective jet Reynolds number along with its downward momentum. In Fig. 2.9 the individual mass flow of the jets with an ArcConic are normalized by the according smooth jet mass flow. The mass flow is averaged in a  $y$ - $x$  plane at a distance of  $3.2D$  from the target plate. The jet is arbitrarily defined as the region in that plane with a downward velocity  $u_x > 5.5m/s$  (0.54% of the average jet velocity). The additional mass flow reduces the jet deflection, shifting the stagnation points upstream. This is visible for all ArcConic configurations in Fig. 2.7. If the rib is not very large, the distribution of jet Reynolds number from the plenum remains unchanged (Fig. 2.8).

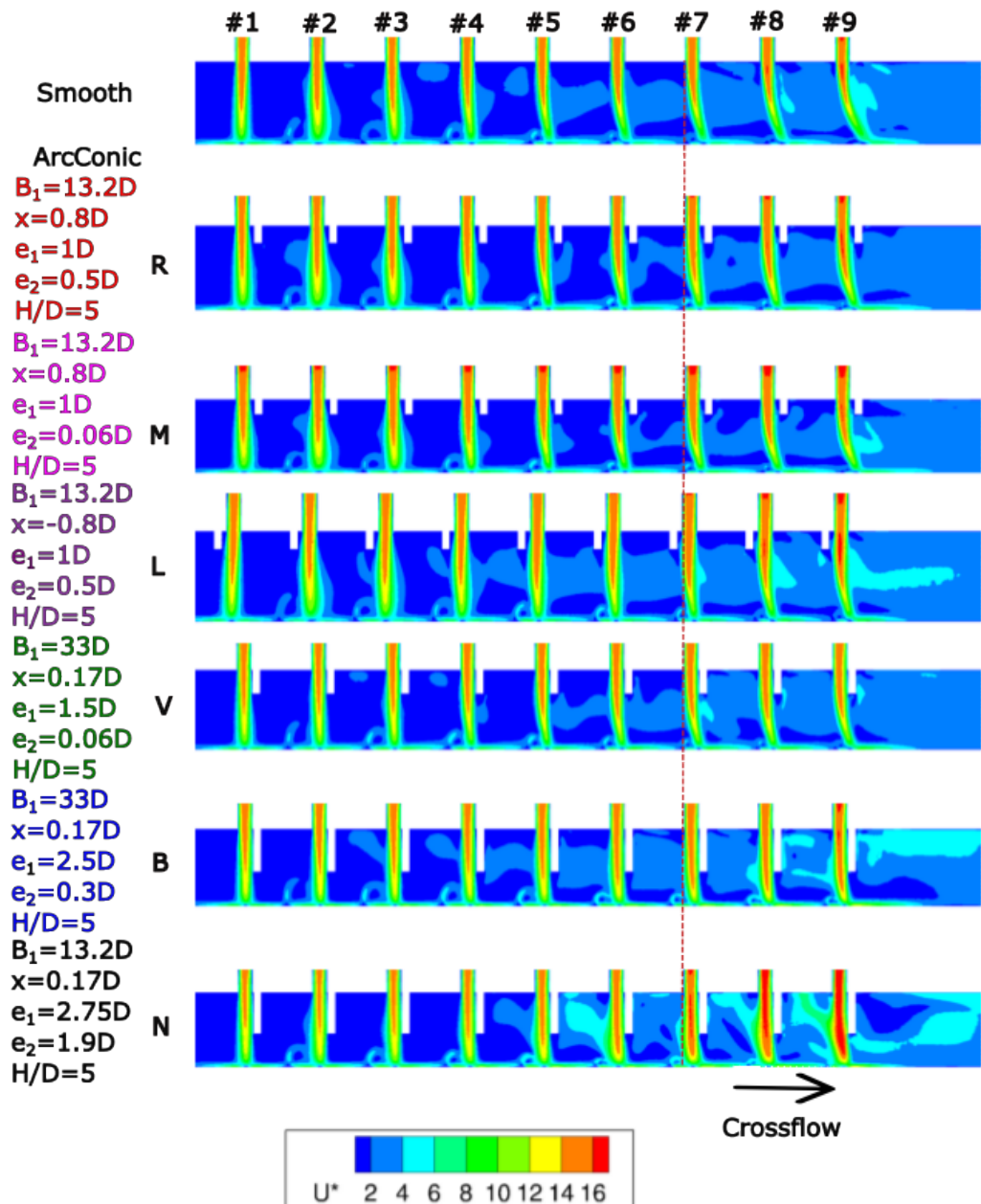


Figure 2.7: Velocity magnitude in the center plan

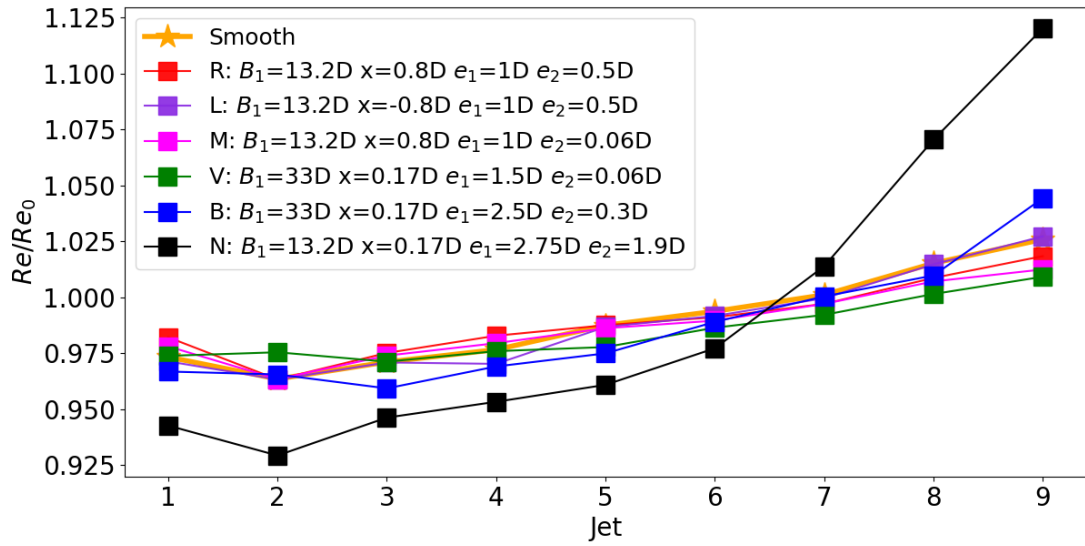


Figure 2.8: Effective individual jet Reynolds number fraction normalized by  $Re_{mean} = 10,000$

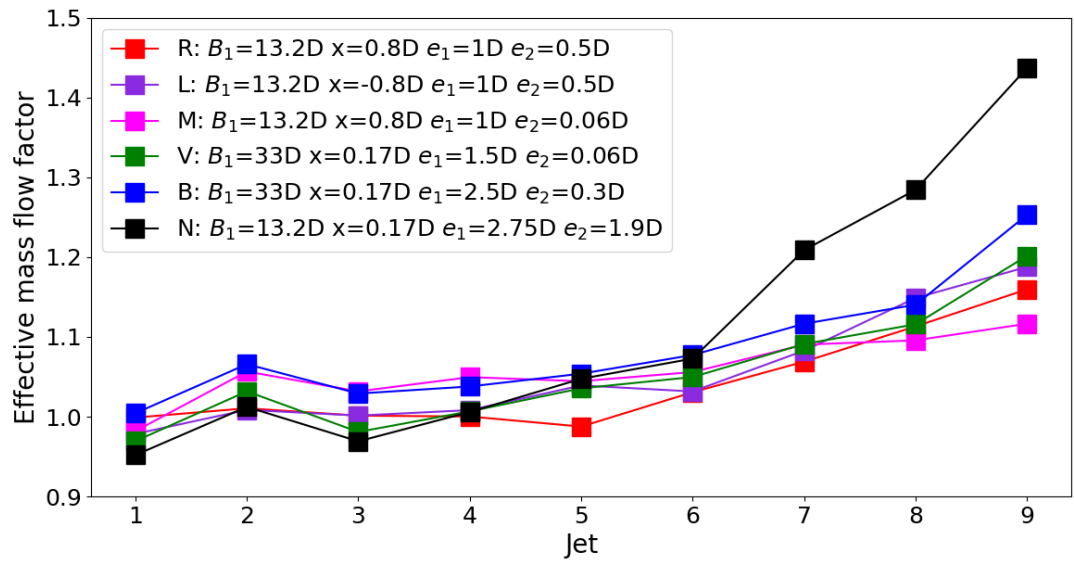


Figure 2.9: Effective jet mass flow distribution,  $Re_{mean} = 10,000$

### 2.3.3 Heat transfer

Figure 2.10 shows the normalized  $Nu$  number on the target plate for the baseline configuration and selected ArcConic configurations. The geometric jet center is depicted by the red dot. The highest heat transfer is reached directly at the stagnation point where the thermal boundary layer is still very thin, causing large temperature gradients. In the radial direction, the thickness of the boundary layer increases and the heat transfer decreases. The cross-flow deflects the impingement jet and disturbs the stagnation region (Fig. 2.7). This delays the impingement in downstream direction and leads to a reduced heat transfer in the stagnation zone for the more downstream jets. Cross-flow effects reshape the impingement jet's  $Nu$  number footprint from a round to a crescent moon shape.

For the ArcConic, the general effects are similar, but more fluid is routed into the downstream jets. Downstream of jet #5, the effects of the ArcConic become visible. The jet deflection of the ArcConic configurations is reduced, the footprint of the jet is moved upstream and the  $Nu$  number is enhanced. For bigger ribs (**V**, **B&N**), the jet footprint is almost directly under the jet hole. In the spanwise averaged evaluations of the Nusselt number shown in Fig. 2.12, the reduced jet deflection and enhanced stagnation  $Nu$  number become very visible. Especially for the configurations with a bigger rib (**B&N**) there is nearly no jet deflection and the jet impinges directly under the jet hole. The stagnation points  $Nu$  number is enhanced by up to 40% for the downstream jets. A degradation of the Nusselt number peaks for the more downstream jets is not visible, the Nusselt number distribution is more homogeneous over all jets.

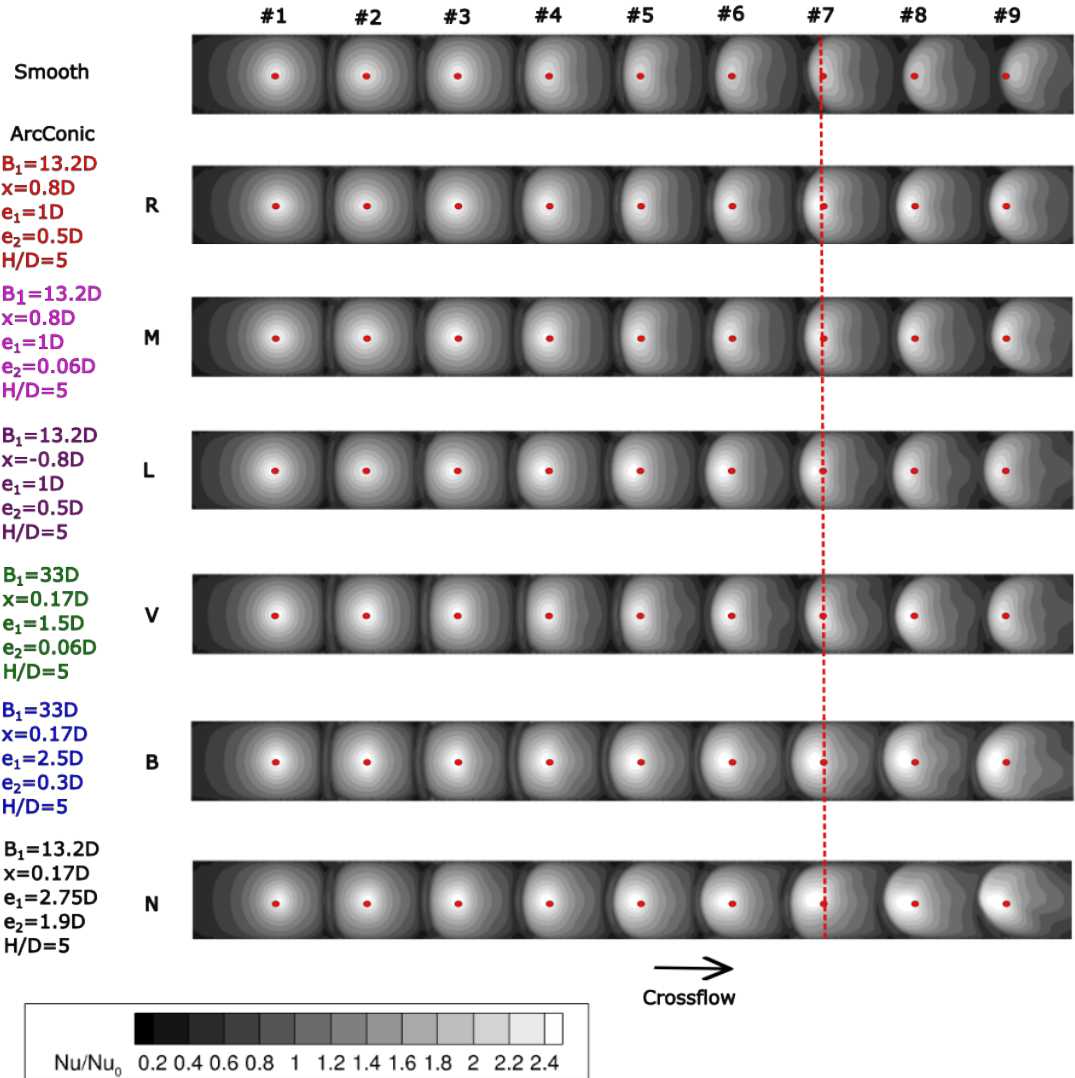


Figure 2.10: Local Nusselt number distribution on the target plate, the red dots indicate geometric jet centers,  $Nu_0 = 45$

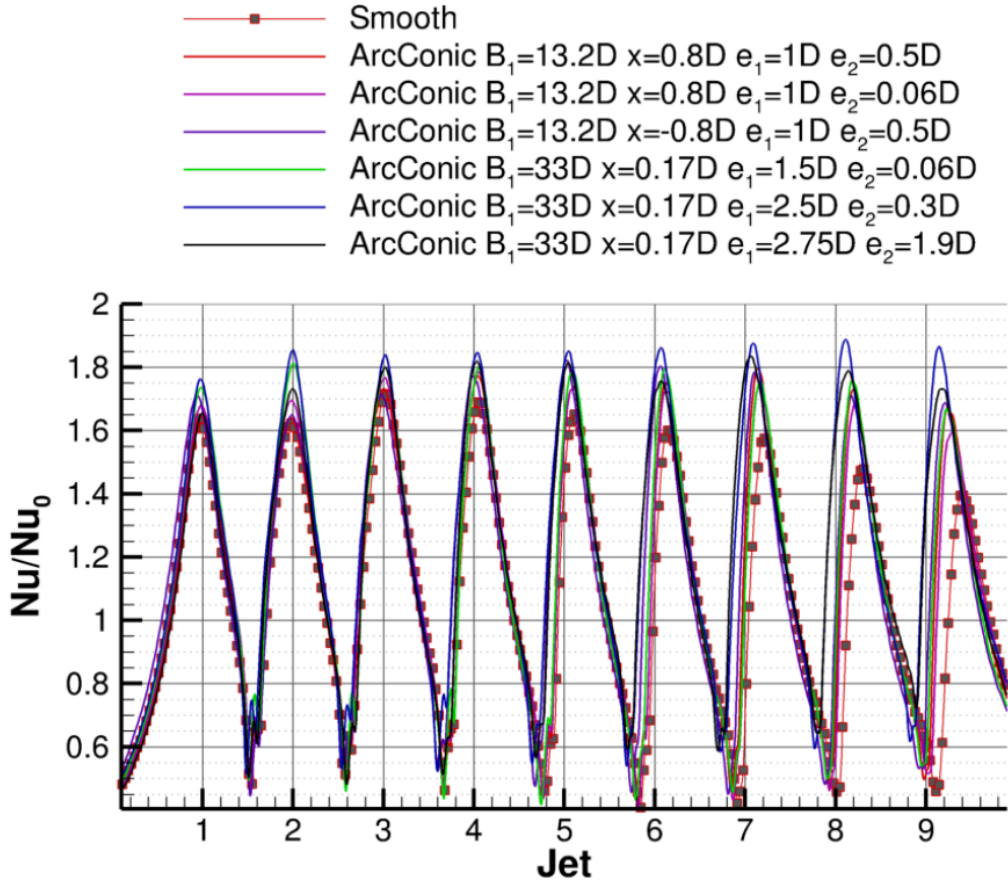


Figure 2.11: Spanwise averaged Nusselt number normalized by  $Nu_0$ ,  $Nu_0 = 45$

### 2.3.4 Effect of Reynolds number

The scalability ( $Nu \propto Re^n$ ) of the Nusselt number and Reynolds number is an important factor for cooling systems, allowing for a comparison with other data from literature. Figure 2.12 shows the spanwise averaged Nusselt number for the smooth and ArcConic configurations with Reynolds numbers ranging from 10,000 to 40,000. With an exponential factor  $n = 2/3$ , the values for the ArcConic agree well with the values for a smooth configuration, also reported in literature. Furthermore, the behaviour of the ArcConic configuration is self-similar regarding the Reynolds number. Hence, the focus of the further discussion will limited to  $Re = 10,000$ .

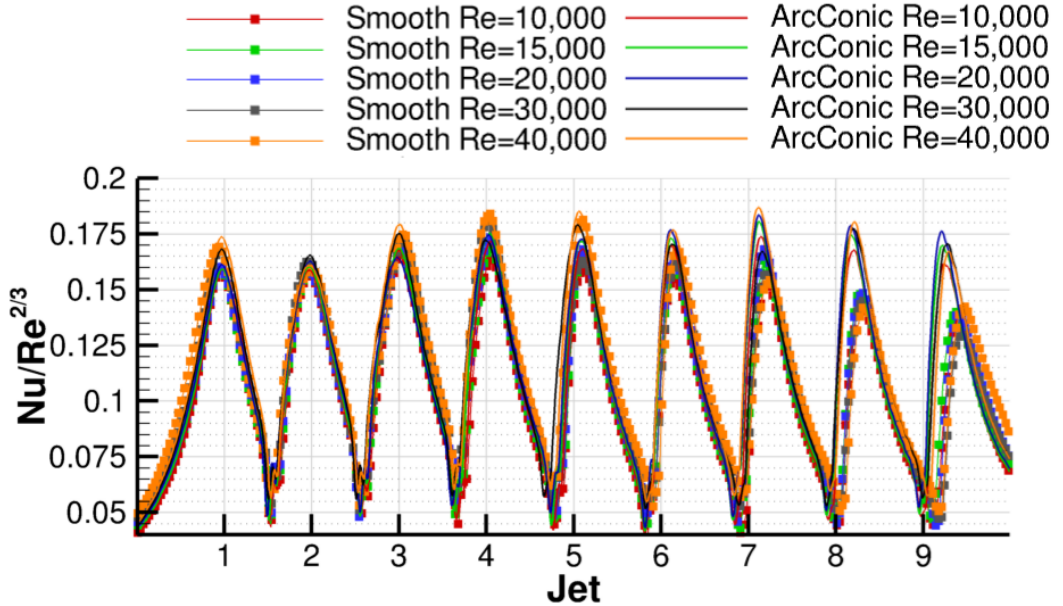


Figure 2.12: Effect of Reynolds number, nornalized spanwise averaged Nusselt number by  $Re^{\frac{2}{3}}$

### Effect of rib position ( $x$ )

Figure 2.13 shows the effect of the streamwise ArcConic placement ( $-0.3 D < x < 1.5 D$ ) on the  $Nu$  number and pressure loss, for different configurations. For points connected by a line, only the the position  $x$  is altered. A higher  $Nu$  and  $C_d$  ratio is desirable in regard to the cooling performance - meaning increased heat transfer and decreased pressure loss. A slight decrease in  $Nu$  and  $C_d$  ratio is visible for increasing  $x/D$  values. The further away the rib is from the hole the less fluid is guided into the jet. For the initial ArcConic configuration (**R**) the Nusselt number ratio varies from 1.06 to 1.03. The  $C_d$  ratio decreases between 0.99 and 0.95. For a bigger rib **V,B & N** a position closer to the jet hole leads to significant increase in heat transfer as more air is guided into the jet. The effect rapidly drops for greater vales of  $x/D$ . The  $C_d$  ratio decreases for a the bigger rib at close distance from the jet hole as the redirection of (more) fluid costs energy. An upstream rib position (**L**) does not significantly change the rib performance. This option was not further explored during this investigation. The rib position  $x$  has only secondary effects on the  $Nu$  number (for small ribs).

Overall smaller values of  $x$  seem slightly beneficial for the rib performance. From a manufacturing perspective, a larger value of  $x$  would be favourable.

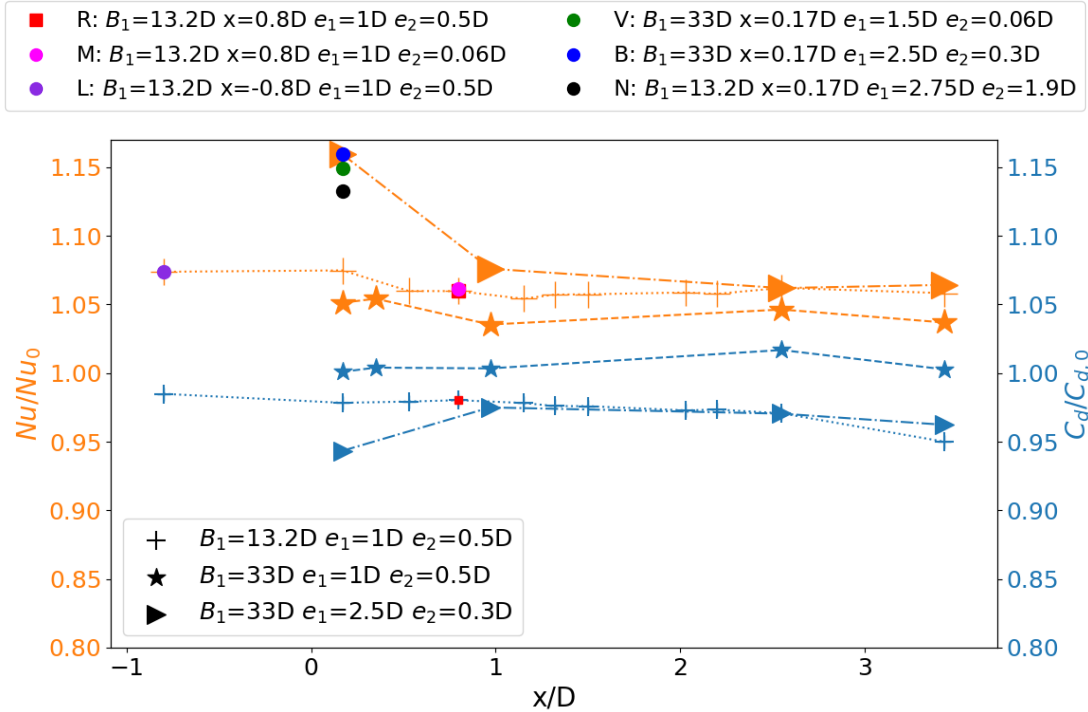


Figure 2.13: Effect of the rib position  $x/D$  on  $Nu/Nu_0$  and  $C_d/C_{d,0}$ ;  $Nu_0 = 45$ ,  $C_{d,0} = 0.62$ ,  $Re = 10,000$

### Effect of rib height ( $e_1$ )

The effect of the variation of the rib height  $e_1$  (with constant  $e_2$ ) between  $0.5D$  and  $4D$  is visible in Fig. 2.14. An increase of rib height  $e_1$  leads to a higher  $Nu$  number and a lower discharge coefficient as more fluid is redirected into the jet (high flow deflection leads to higher pressure loss). There is an additional blockage effect in the channel due to the bigger rib (N Fig. 2.7). The re-circulation zone upstream of the jet is bigger because the larger rib hinders jet deflection. Due to the blockage effect, the cross-flow velocity increases. This results in a small but visible decrease of static pressure in the channel with more air being drawn into the downstream jets (B and N Fig. 2.8). Also, the bigger rib redirects more cross-flow air into the jet(B and N

Fig. 2.9). Both effects are beneficial for heat transfer but also lead to higher pressure loss. The rib size is limited by the channel, the  $Nu$  number augmentation seems to plateau at about 16%. The configuration **V** has a medium size ArcConic ( $e_1=1.5D$ ) that is very small near the edges ( $e_2=0.06D$ ), this configuration offers high Nusselt number augmentation (14%) at nearly no pressure penalty ( $C_d/C_{d,0}=0.99$ ). Maximum heat transfer obtained by the biggest rib, has an increase of 16% with an increase of 9% in pressure loss. The effects of the ArcConic are mainly driven by the height of the rib  $e_1$ .

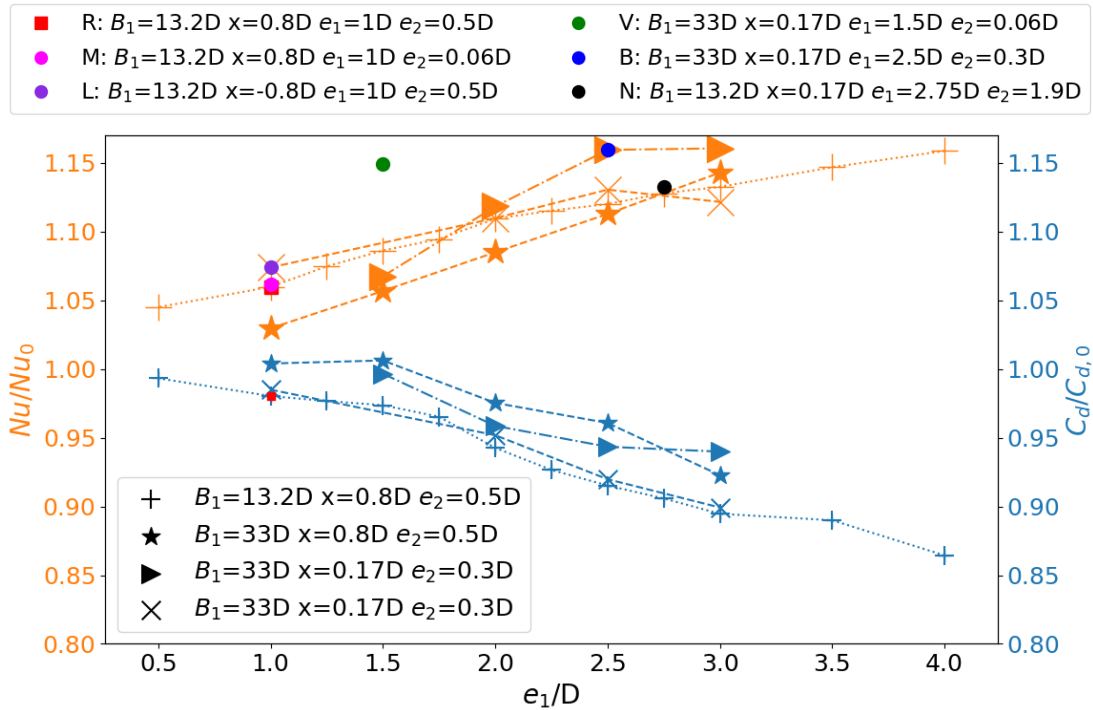


Figure 2.14: Effect of rib height  $e_1/D$  on  $Nu/Nu_0$  and  $C_d/C_{d,0}$ ;  $Nu_0 = 45$ ,  $C_{d,0} = 0.62$ ,  $Re = 10,000$

### Effect of rib length ( $B_1$ )

Figure 2.15 shows a variation of length of the ellipse  $B_1$  between  $13.2D$  and  $39.5D$ , with a constant position  $x$ . The rib length also defines its curvature. A longer rib offers a smoother guiding of the flow into the jet with a small but positive effect on the pressure loss. Heat transfer is not significantly influenced by the length of the

ellipse  $B_1$ . For the initial ArcConic configuration (**R**), the  $Nu$  number augmentation is between 2% and 6% while the discharge coefficient ratio varies between 0.97 and 1.02. Please note that a value of 1.02 means a decrease the pressure loss compared to the smooth configuration. This small positive effect is probably caused by prohibiting the re-circulation area directly downstream of the jet hole. Negative effects on the pressure loss like sharp curvature or bigger rib are stronger and superimposed in the other configurations.

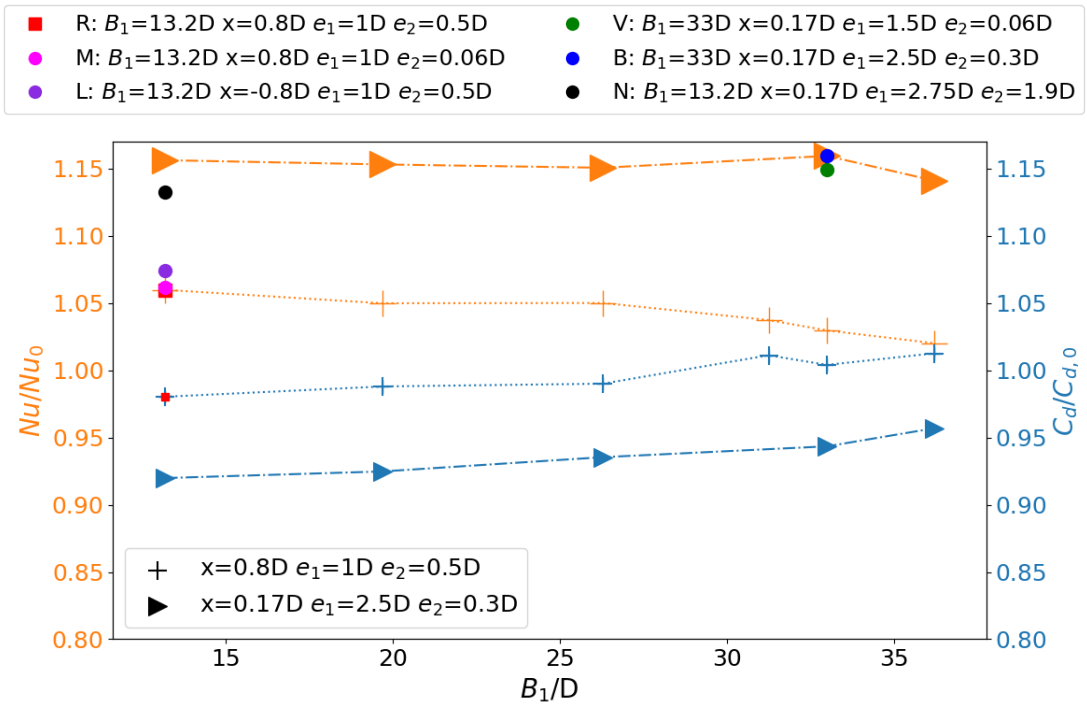


Figure 2.15: Effect of rib length  $B_1/D$  on  $Nu/Nu_0$  and  $C_d/C_{d,0}$ ;  $Nu_0 = 45$ ,  $C_{d,0} = 0.62$ ,  $Re = 10,000$

### Effect of rib shape ( $e_2$ )

A variation of the rib shape factor between  $0.07 D < e_2 < 1.22 D$  is depicted in Fig. 2.16. With increasing  $e_2$ ,  $C_d$  slightly decreases and  $Nu$  slightly increases. The rib gets bigger on the sides and offers more flow resistance. However, more fluid is scooped into the jet, which increases heat transfer. Smaller values for  $e_2$  seem to be favourable. However,  $e_2$  does not have a major effect on the rib performance. For the

initial ArcConic configuration (**R**) the  $Nu$  number augmentation is between 6% and 9% while the discharge coefficient ratio varies between 1.05 and 1.00. The positive effect of the small  $e_2$  values is probably caused by prohibiting the re-circulation area directly downstream of the jet. However, as less cross-flow air is guided into the jet, the  $Nu$  number enhancement becomes smaller. From a manufacturing point of view a larger value of  $e_2$  would be favourable.

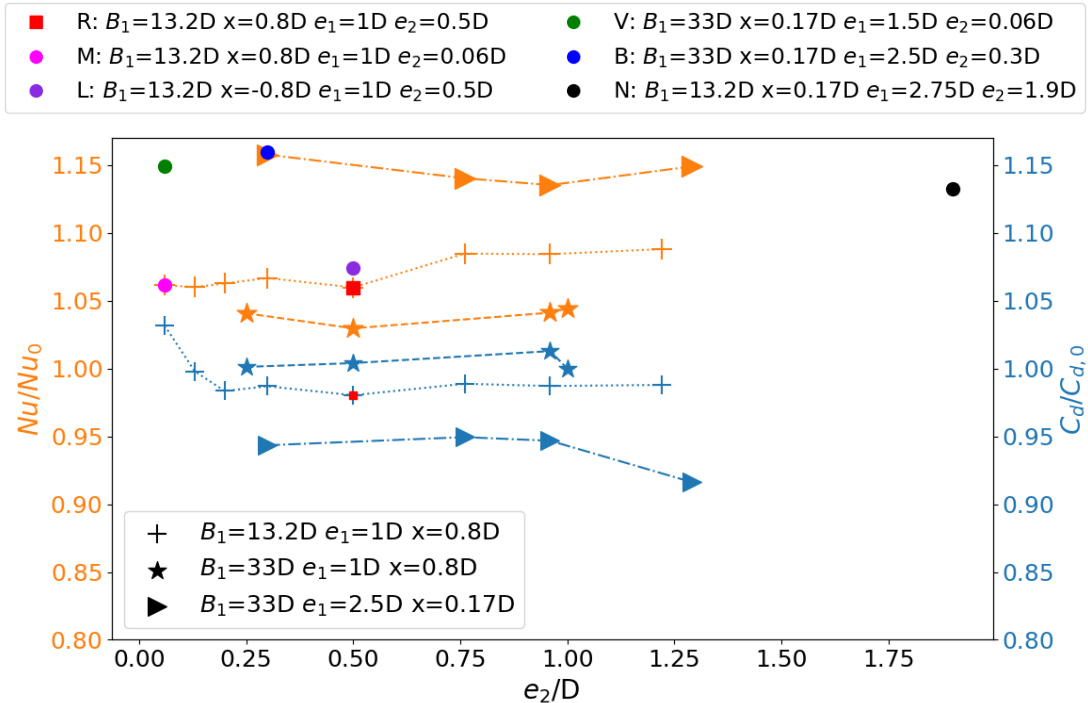


Figure 2.16: Effect of rib Sharpe  $e_2/D$  on  $Nu/Nu_0$  and  $C_d/C_{d,0}$ ;  $Nu_0 = 45$ ,  $C_{d,0} = 0.62$ ,  $Re = 10,000$

### Effect of separation distance ( $H/D$ )

The area averaged  $Nu$  number and discharge coefficient for various separation distances ranging from  $H/D = 2$  to  $H/D = 5$  are depicted in Fig. 2.17. Values are normalized against data from a smooth channel configuration. The smaller separation distances lead to higher self-induced cross-flow velocities, beneficial to heat transfer augmentation of the ArcConic. However, the relative rib height  $e/H$  increases and leads to a blockage effect which drastically increases the pressure loss. The gain in

heat transfer does not justify the increase in pressure loss for the small separation distance of  $H/D=2$ . The same pressure penalty in smooth configuration would lead to higher Reynolds numbers and higher heat transfer (Fig. 2.7). The ArcConic is also effective on smaller separation distances, but for  $H/D < 3$  the pressure penalty becomes prohibitive.

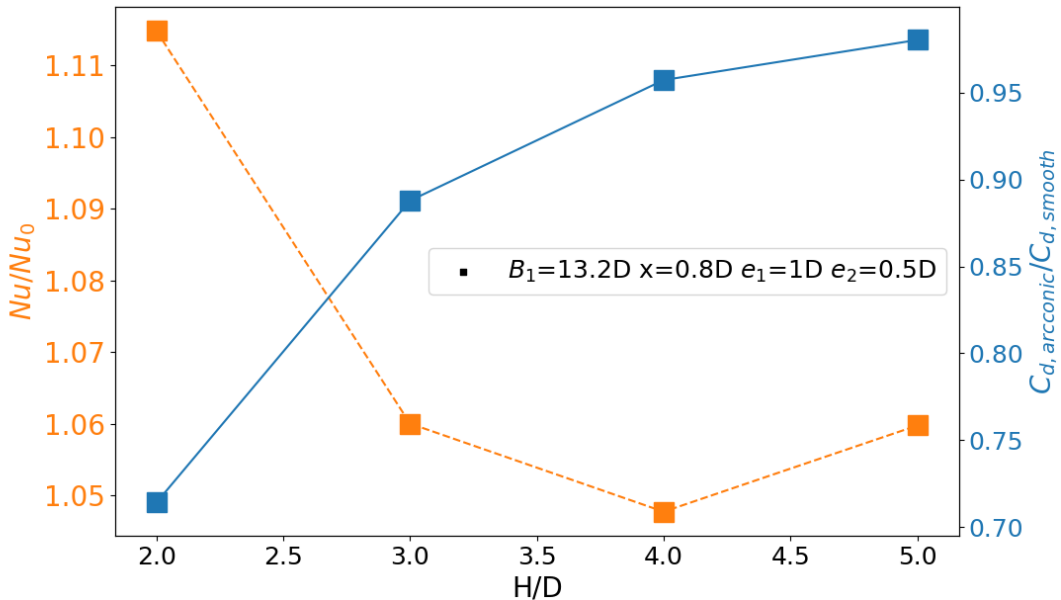


Figure 2.17: Effect of separation distance  $H/D$  on  $Nu/Nu_0$  and  $C_d/C_{d,0}$ ; normalized by the according values for the smooth configuration

### 2.3.5 Combination with other features

To further increase heat transfer, additional surface modifications can be added to the target plate. A good candidate may be a micro pin fin pattern, effective due to an area increase and by breaking and restarting the thermal boundary layer [8, 61]. In a similar impingement cooling configuration with a smooth hole plate and a micro pin fin surface modification on the target plate, an area increase of 50% results in a heat transfer increase of 42%. This feature is mostly effective due to the area increase and could be used in combination with an ArcConic configuration to additionally use the cross-flow potential. The micro pin fin pattern requires no exact alignment with the jet. Another possibility is to add concave dimples [73] to

the target plate, placing the center exactly under the jet hole. The concave curvature accelerates the wall jet which is beneficial for heat transfer. With a dimple diameter of  $1.8D$  and a dimple depth of  $0.15D$ , an additional  $Nu$  number augmentation of 12% could be reached. The surface area of the modified target plate would increase by 26.4%, further increasing the total heat transfer. The alignment of the jet with the dimple is critical. The ArcConic would decrease the jet deflection, which would help with the performance of the dimple. Longitudinal ribs or V-ribs ([14]) can be used to protect the stagnation zone from the adjacent wall jets, guide the flow around the jet and increase the heat transferring area. A V-rib with a square cross-section ( $w/D = e/D = 0.5$ ) and an opening angle of  $90^\circ$  placed upstream of the stagnation zone increases the heat transfer by 23% [14] and could be used together with the ArcConic.

## 2.4 Manufacturability

A key requirement for real world application of the ArcConic is scalability. The jet hole diameter  $D$  should reach values down to 1 mm. Additive manufacturing may enable such scalability. Let us consider two scenarios for a practical application in an aero-engine high-pressure turbine first stage: a ceramic matrix composite (CMC) vane with an impingement insert and a full SLM blade with built-in impingement cooling. CMC enables considerably higher service temperatures [52] at the expense of geometry complexity. Based on a concept developed by GE, a CMC shell can be combined with an SLM impingement insert [66, 67]. Adding the ArcConic to the insert, further enhances internal cooling efficiency. To offset the lower service temperature of Ni-based alloys, the downstream blade may be additively manufactured to enable higher complexity and higher efficiency cooling geometries. In particular, the inline impingement cooling configuration at the leading edge of a state-of-the-art blade [59] may be upgraded with the ArcConic.

The advent of additive manufacturing technologies has revolutionized several industries and laser-based techniques, such as selective laser melting (SLM), have been recently explored to manufacture turbomachinery components [25]. Benefits include complex cooling geometries [44], lower lead times and significant component simplifi-

cation [55, 4].

The SLM of Inconel (IN) 625 or 718 has reached a high technology readiness level (TRL) and has been the object of various experimental investigations [65, 35]. In particular, the low amount of Ti and Al in IN718 gives it excellent weldability properties, essential for SLM. However, the hardening  $\gamma''$  phase begins to coarsen at high temperatures, limiting its service temperature to 920–970 K [50, 21]. This is a possible deal breaker for the high-pressure turbine hot environment. Switching to  $\gamma'$  strengthened alloys (higher Ti and Al content), such as IN939, enables service temperatures up to 1120 K [22] at the expense of welding and crack-free properties [50]. Despite these challenges, cooled IN939 SLM blades have already been demonstrated in commercial gas turbines, reaching a TRL of 7 [23].

In terms of quality control of SLM turbine blades, key aspects are: (i) the surface quality, which can directly affect the fluid dynamic performance, and (ii) the characterization and resolution of the micro-structures [19, 43].

A post-processing by hot isostatic pressing, for instance, has been recently proved to reduce residual porosity and surface defects in equiaxed-grain Inconel microstructures [41]. In addition, by optimising the processing parameters, *in primis* power, scan speed and spot size, surface roughness can be controlled and reduced to bellow 3  $\mu\text{m}$  [5, 56]. Note that a controlled surface roughness can be beneficial for increasing heat transfer [60]. However, surface roughness is also dependent on the printing direction [21, 22]. Post-processing techniques like pulsed electro-chemical machining or shot peening can solve this problem [1, 42], depending on the access to the surface in question.

Commercial SLM machines can now reach printing heights up to about 1.0 m and feature sizes as low as 50  $\mu\text{m}$  [2, 26]. However, a large printing volume and a high printing resolution are usually competing features. SLM could be a viable manufacturing process for a high-pressure turbine blade or for a metallic insert with integrated ArcConic, under certain conditions. For instance, the distance  $x$  and the dimension  $e_1 - e_2$ , displayed in Figure 2.1, are critical geometrical parameters which can hardly be manufactured below a certain threshold. Assuming  $D \approx 1 \text{ mm}$ , a reasonable lower

bound for a successful high-quality manufacturing by SLM could be  $x > 0.7D$ . In addition, the difference between  $e_1$  and  $e_2$  can be successfully realised only if it is sufficiently large, e.g.  $(e_1 - e_2) > 0.2D$ , otherwise a rib with an approximately constant height is obtained. Note that these order-of-magnitude estimations may change depending on the machine and processing parameters.

In short, a trade-off between thermal-fluid dynamic performance and manufacturability is expected. Future work should be directed at evaluating the manufacturability by SLM of the full turbine blade or impingement insert incorporating the presented Arc-Conic. Different printing orientations should also be investigated in order to evaluate their effect on the surface roughness and material density of the alloys of interest.

## 2.5 Conclusion

The present work numerically investigates ArcConic configurations installed downstream of the jet hole of an impingement cooling system in maximum cross-flow condition. The arrangement uses the cross-flow to reinforce the jet and thus increase the heat transfer on the target plate. A single operating condition with a jet exit Reynolds number of 10,000 is analysed in greater detail. A profound parameter analysis is performed to identify geometric effects on heat transfer and pressure loss. The following conclusions can be made regarding the ArcConic in an impingement cooling configuration:

1. The average Nusselt number on the target can be increased by up to 16% depending on the specific geometry, while pressure loss can increase by around 6%. In the stagnation points,  $Nu$  number enhancements are in the range of 40%.
2. The Nusselt number distribution is more homogeneous and a degradation of the Nusselt number peaks for the more downstream jets due to cross-flow does not occur.
3. A larger rib height leads to a higher heat transfer and pressure drop.

4. As the target plate is not modified, the ArcConic can be combined with other area increasing turbulators on the target plate to further increase heat transfer.
5. Manufacturability via SLM may be a viable solution for Inconel alloys. Based on the resolution of available commercial machines, a compromise between the refinement of the geometrical parameters and the thermal-fluid dynamic performance is expected. For example, the Nusselt number enhancement obtained by placing the rib closer to the jet can be partially restricted due to a minimum required distance for manufacture.
6. Future work will include an experimental validation as well as the formulation for a correlation for the pre-design of a cooling system for turbomachinery application.

# **Chapter 3**

## **Conclusion**

# **Appendix A**

## **Impingement jet cooling**

### **A.1 Impingement Jet Cooling**

On gas turbine, the turbine supported a high temperature in order to improve the overall efficiency, but the high temperature created by the combustion can damage the turbine blades and so, gas turbine. Despite the improvement of the material thermal properties, the turbine blade must be cooled in order to limit the damage. Jet impingement cooling is frequently used in on the leading edge and the mid-chord as it offers high transfer rates with efficient usage of coolant.

#### **A.1.1 The Single Impingement Jet**

Basic knowledge of the physical phenomena is essential to understand the multi-jet. An impinging jet is consisting of three characteristics regions namely free jet region, stagnation region and wall jet region, as shown in Figure A.1.

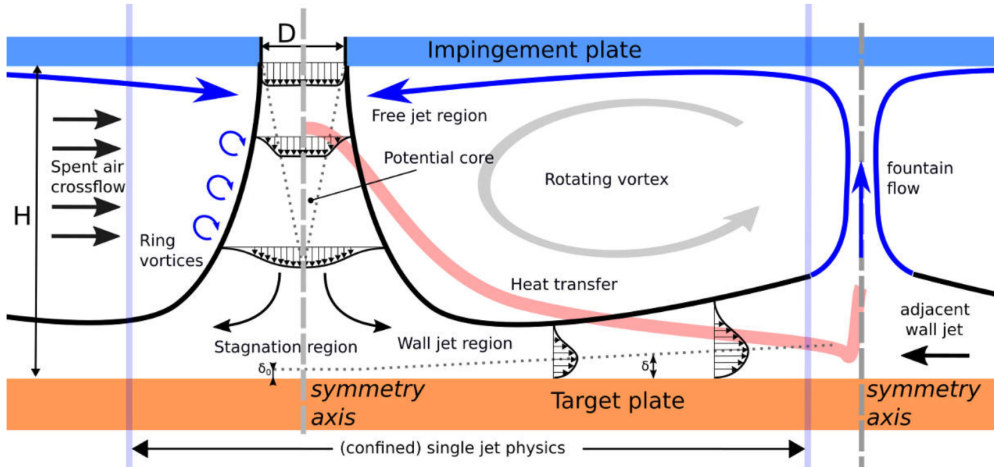


Figure A.1: Impingement jet flow-structure [7]

In the **free region**, the jet is not affected by the plate, thus the jet behaves as a free submerged jet. After the jet meets the ambient fluid, it develops the shear regions. N. Zuckermann and N. Lior [76] explained that the shear layer grows along the axial of the jet and can cause an instability or turbulence. The free region grows, it stretched the ring vortex and generated turbulence as shown in Figure A.1 in blue. The velocity decreases around the center because there is an apparition of vortexes and so, decreases the pressure. The potential core is the flow interior which is unaffected by the turbulence because the velocity is close to the velocity at the nozzle exit. Moreover, the potential core can extend to 6 to 7D from the nozzle [7] because the velocity decreases until the point where the velocity profile is fully developed. Before the jet is characterized as a fully developed, it was self-similar free jet. At a distance of  $2.5D$  from the impinging plate the velocity is considered as self-similar, similarly for the turbulent quantities at  $4.5D$  [39]. When the jet enters in the **stagnation region**, the flow is near the target plate. The axial Velocity component decreases until reaching zero as stated B. Weigand [69] and the static pressures increases. The high static pressure in the stagnation region accelerates the fluid in radial direction and forms the **wall jet**. The **wall jet region** will be first laminar due to the acceleration and eventually become turbulent. In the stagnation region, the boundary layer has a thickness  $\delta_0$  of  $0.01D$  or less. The **wall jet** has two

shear layers, one at the target plate and one at the interface to the surrounding fluid. The acceleration cause both shear layers to grow. This cause the turbulence level to be higher. The boundary layer grown and defined the region where the velocity reaches a maximum. The wall jet velocity reaches a maximum at 1D [69] from the stagnation point. Around the stagnation point, the region has a maximal transfer in heat [46]. But, as seen in Figure A.1, the velocity profile develops and expands due to the viscous forces, and so decreases the velocity. The mass conservation decelerates the jet, and so there is the transition when the acceleration has disappeared.

### A.1.2 Multi-jet impingement

The heat transfer in multi-jet arrays is generally similar to the single jet impingement with some additions. Indeed, the multi-jet impingement may be influenced essentially by two different kinds of interactions. First is the jet-jet interaction preceding the impingement on the surface. It reduces the strength of the jet, and shortens the potential core; and so, degrade the efficiency of the heat transfer. Second type is the collision of the flow from the adjacent jet, among the wall jets of impingement jets after their impingement on the target plate. It generates fountain as illustrated on Figure A.1. Thus, a secondary stagnation region emerges due to the collision and there is degraded on the heat transfer performance.

We used turbulators in order to limit these phenomena that affected negatively the heat transfer. Indeed, turbulators is an element adding on the hole plate or/and the target plate in order to enhance the heat transfers. Then, I will present the different turbulator for the heat transfer enhancement.

# **Appendix B**

## **Turbulator**

### **B.1 Turbulator**

The crossflow generated by the multi-jet configuration can damage the overall efficiency. In order to reduce the unfavorable effects of the crossflow, turbulators are frequently used because turbulator consists of enhancing the heat transfer by reducing the low heat transfer regions with different methods.

It exists different turbulators as such pin-fin, ribs, detached ribs and other. All of them have different methods in order to improve the heat transfer, indeed, they can enlarge area and/or block crossflow and/or guide the flow. However, for some turbulators, the pressure loss increases which reduces the efficiency of the methods.

#### **B.1.1 Pin-Fin Turbulator**

Due to the manufacturing constraints on the trailing edge, pin-fin turbulators are used to enhance the heat transfer. But, this technique can be coupled to the impingement jet cooling. Therefore, pin-fin turbulators can be located on the target plate or the hole plate in order to increase surface area and turbulence.

As the coolant air pasts through the pin-fin array, the flow separates and wakes

are shed downstream of the pin. In addition, a horsevortex is formed upstream of the pin base and results on two counter-rotating vortex forming the secondary flow downstream of the pin-fin due to the separation of the flow as shown in Figure B.1. All of this enhance the heat transfer and reduce the boundary layer due to the secondary flow. Indeed, the secondary flow allows to enhance the heat transfer due to turbulence. There are different studies that explain how the pin-fin can improve the heat transfer. Indeed, the geometry recommended is rectangular or cylinder [7] but, it exists different geometry like diamond shape pin-fins [72]. But, each type of pin-fin have a different effect on the heat transfer [72]. However, all studies explains that the principal effect of the pins is to interact with the crossflow in order to generate the enlarge surface and turbulence in the wake region behind the pins.

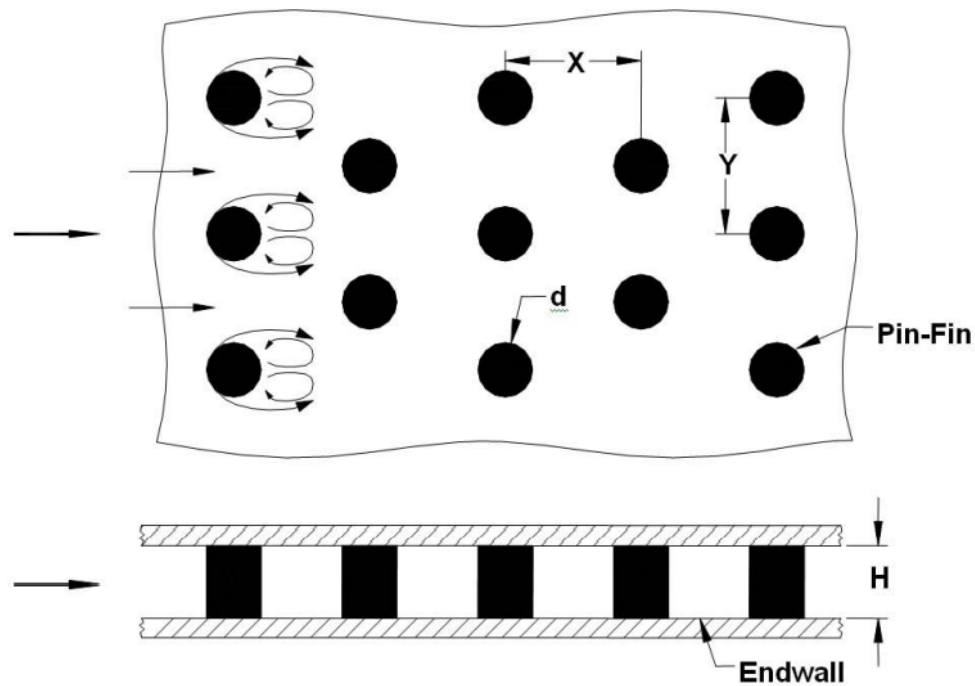


Figure B.1: Structure flow in pin-fin channel

### Pressure loss and heat transfer

R-G. Brakmann [7] studies drop pressure and heat transfer for a 9x9 jet array on a target plate composed of micro cubic pin-fins. The pressure loss increases by 5% to 3%

compared to the smooth plate configuration. The impingement on the target plate, the interaction of the jet with the crossflow and the interaction of the crossflow with the Pin-Fin itself each effect the pressure loss. Therefore, the pin-fin will interact with the crossflow and so, increases the pressure loss. When the surface area are included, the Nusselt number decreases slightly due to the vortex downstream of the jet. But R-G. Brakmann [7] explained that the Pin-Fins increase the target area by a factor of 1.5 relative to a flat plate. So, the enlarged area increases the convective heat transfer.

### B.1.2 Dimples

Dimples have been considered as an alternative to pin-fin cooling and usually located on the target plate. They generate a low pressure penalty and moderate the heat transfer enhancement. Figure B.2 shows the flow structure with dimples, and so the dimple induced a secondary flow. The dimples induced a separation flow which generated recirculation area and reattachment with pairs of vortices. The secondary flow induced by the pairs of vortices. Dimples generate swirling flows and turbulence, and so enhance the heat transfer. However, the dimple size, dimple depth, distribution and shape each effect the heat transfer distribution in the channel.

#### Pressure loss and heat transfer

J-C Han and L. M. Wright [72] explain that the heat transfer in the dimpled channel is typically 2 to 2.5 times greater than smooth channel with a pressure loss penalty of 2 to 4 times of a smooth channel. The area of high heat transfer corresponded to the area of the flow reattachment directly downstream of the dimple. In addition, the pairs of vortices generated in dimple allow to enhance the heat transfer on the target plate. The pressure loss is generated by recirculation area formed by the flow separation.

### B.1.3 V-rib Turbulator

In opposition to pin-fin, V-Rib turbulators have a blockage effect on the crossflow, in addition to enlarging the surface area. This technique is usually used in the internal

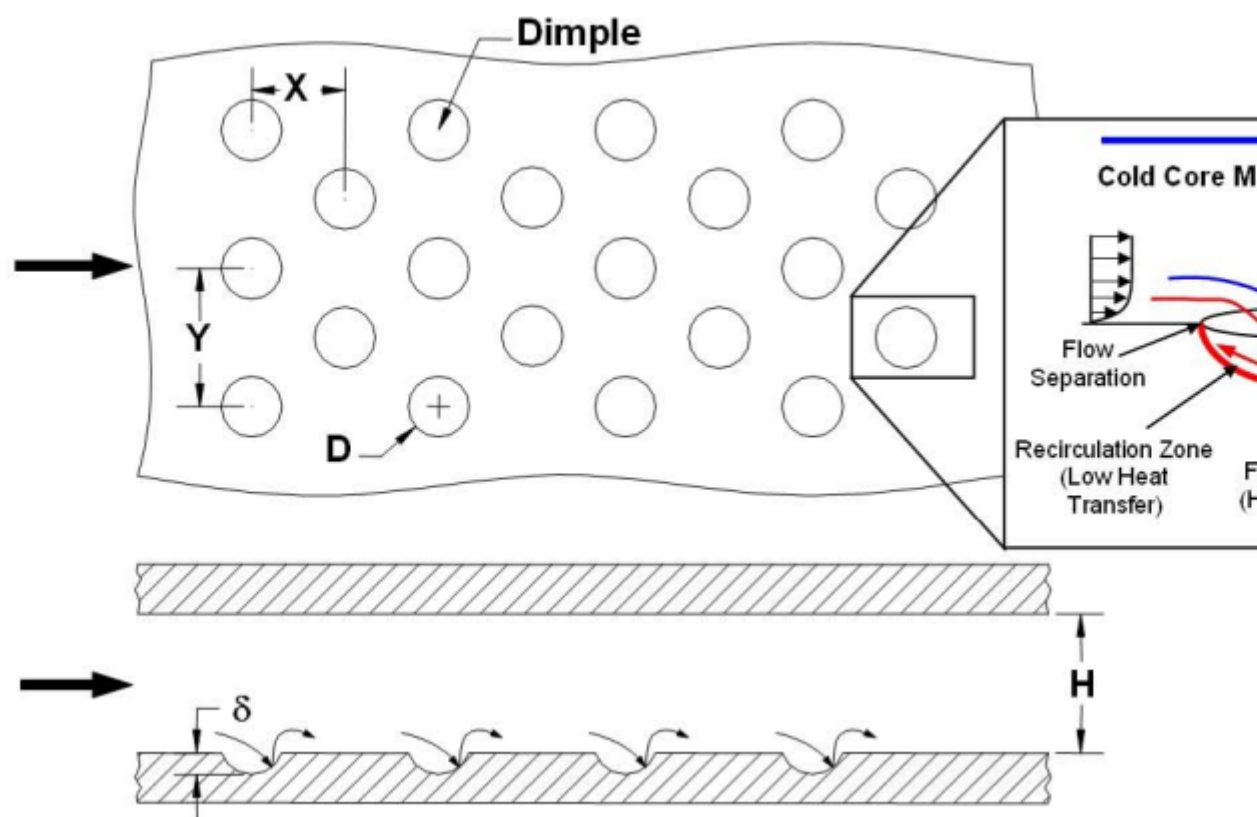


Figure B.2: Structure flow in dimples channel

serpentine cooling channel, but it is also coupled to the impingement jet cooling. The ribs are located on the target plate or/and the hole plate. The V-Ribs on the target plate protect the impingement jet from the crossflow and the V-Ribs on the hole plate reduce the channel area where the crossflow evolved. As the coolant air passes over a rib, the flow is separated and a closed recirculation zone is formed downstream of the jet as illustrated in Figure B.3. This region is characterized by two counter-rotating vortex pair. Then, the flow is reattached before the next rib. The ribs formed a secondary crossflow due to the to the counter-rotating vortex generated downstream. In the presence of V-Ribs, the crossflow is redirected away of the jet and so, there is lower of loss of jet kinetic energy. This allow to increase the heat transfer. But, there is different geometry as  $\Delta$ -Ribs, M-ribs and W-ribs [7] [9] [72] that have different effects. But, the best configuration is the V-Rib turbulator because it offers the best performance for the heat transfer.

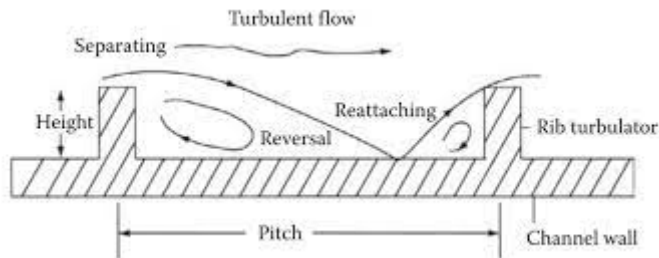


Figure B.3: V-Ribs in flow channel

### Pressure loss and heat transfer

One study of R-G Brakmann [7] is focus on drop pressure and heat transfer for a 9x9 jet array on a target plate composed of V-Rib turbulator only on the hole plate. The pressure loss increases by 4% compared to the smooth plate configuration. The pressure loss is lower compared to the other cases in Chapter V-Ribs in Brakmann's thesis [7]. TH pressure drop is lower because there is a reduction of the open channel area and the induction of the vortex system that prevents the reattachment of the flow on the hole plate. In this configuration, the stagnation region is not protected but the jet momentum increases due to the crossflow and so the jet strength is higher

compared to the baseline case. So the heat transfer increases by a factor 1.06 because the jet deflection is lesser due to an increase in the jet momentum. In this study, the crossflow allows to enhance the heat transfer.

#### B.1.4 Conclusion

All turbulators only slightly increases the pressure drop. So, the crossflow is an undesirable factor which increases the pressure loss. But, for the V-Ribs only on the hole plate, the crossflow is used to improve the heat transfer. Indeed, the crossflow allows to increase the jet strength jet in order to increase the impinging on the target plate and so, increase the heat transfer. But, is it possible to use the crossflow in order to improve the cooling efficiency? In order to respond to this problem/question, the InnoCool project introduces the ArcConic turbulator inspired to the V-Rib turbulator. The work is explained in Chapter 2.

# **Appendix C**

## **Impingement Jet array on Flat Smooth Target (Baseline)**

In this chapter, I will explain the work of Ms Tabassum [58]. To gain a closer insight into the impingement jet physics, she realised Large Eddy Simulations (LES) and measurements from the Particle Image Velocimetry (PIV). Then, she made a comparison between of RANS results with LES data and the experimental data. Firstly, I will explain her experience. Secondly, I will explain the simulations with the comparison. Finally, I will compare my RANS data with RANS data of Ms Tabassum [58].

### **C.1 Experience**

#### **C.1.1 The Particle Image Velocimetry**

The Particle Image Velocimetry PIV is an optical method of flow visualization. It is used to determine all three velocity components and related properties in fluids. The principle of the PIV consists of seeding tracer particles which are assumed to follow the flow dynamics. To extent that a laser points into the fluid and illuminates the particles in order to produce vector fields. A camera CCD allows to save the flow with

two short light pulses at a distance of a few microseconds. The particle ensembles are recorded on two separated images of the camera.

In order to measure the heat transfer, there is different experience model as the Transient Liquid Crystal (TLC). However, the project prefers ...

### C.1.2 Experience Setup

The experimental setup shown in Figure C.1 is an arrangement of nine circular jets, each  $D = 0.0152m$  in diameter, arranged in a row with a jet pitch of  $\frac{p}{D} = 5$  impinging on a heated flat plate. The jets are integrated into a square cross-section channel 2 with a side edge length (height and width) of  $\frac{H}{D} = \frac{W}{D} = 5$  and a duct length of  $\frac{L}{D} \approx 60$ , which is open only at one of the face ends and is placed on top of a plenum 5. At the downstream end, a blower 7 in suction mode generates the flow, drawing atmospheric air from the environment, mixing it with aerosol seeding in a tubular tank with a baffle plate, and evenly distributing it into the plenum 5 by four rakes. For homogenization, the flow passes through a honeycomb structure, three graduated screens, and a nozzle geometry for cross-section reduction before entering the channel through the nine jet holes with a length of 3D. The resulting flow leaving the channel at the open downstream end establishes an increasing crossflow from closed to open face end in the channel. An orifice metering section 6 with sufficient upstream length to determine the mass flow is placed between the channel outlet and the blower. For optical access from all three coordinate axes, four walls of the channel are made of fused silica glass with high optical quality. It was decided to replace the upper heated flat plate with a glass window during the PIV investigations as the influence of the chosen heat quantity on the velocity flow field is considered negligible and the advantage of important optical access is decisive.

## C.2 Numerical Modelling

For modelling turbulence, Ms Tabassum [58] used LES in order to validate experimental results. But, she also used RANS model in order to compare with LES data and the experimental data.

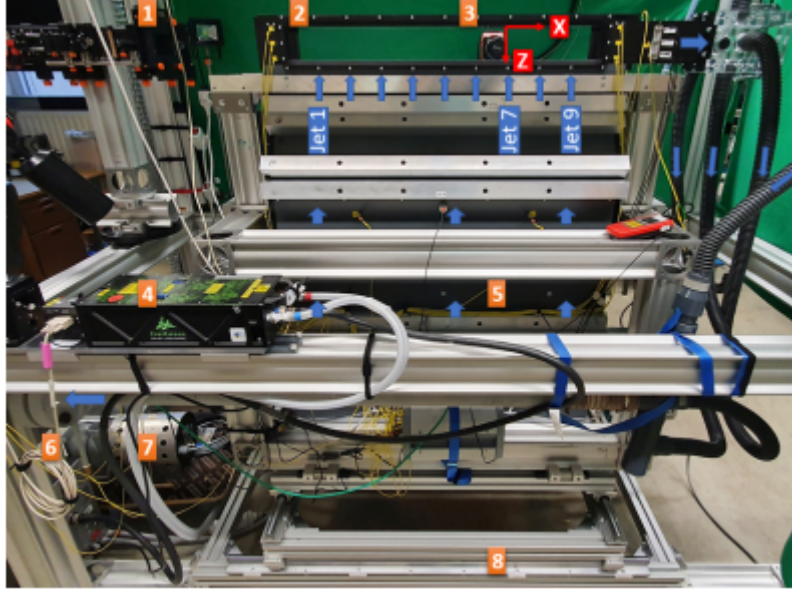


Figure C.1: Experimental Setup  $\frac{2D}{2C} - PIV$  in  $XZ - plane$  orientation showing 1 light-sheet optic, 2 square cross-section channel, 3 SCAMOS camera, 4 laser head, 5 settling chamber, 6 orifice metering section, 7 blower, 8 2-axes traversing unit [58]

The computational domain of RANS and LES simulations is a replica of the experimental setup, with an extended outlet to avoid the reflection of boundary conditions on the jets presented in Chapter 4 section XXX. In contrast to the RANS studies, the plenum was not included in the computational domain.

RANS equations are time-averaged equations of motion flow fluid. It is used for steady problems. In opposition to LES equations, LES equations are local filtering equations and it used for unsteady equations. RANS models have some limitations due to the modelling assumptions.

LES equations are similar to RANS equations but the unknown terms are Sub-grid Scale stresses. The filtering of the equations is obtained at mesh size level, relegating the modelling to flow scales. LES modelling offers increased range of applicability and increased fidelity of the solution but all of this comes with an increased computational cost due to the time step requirements.

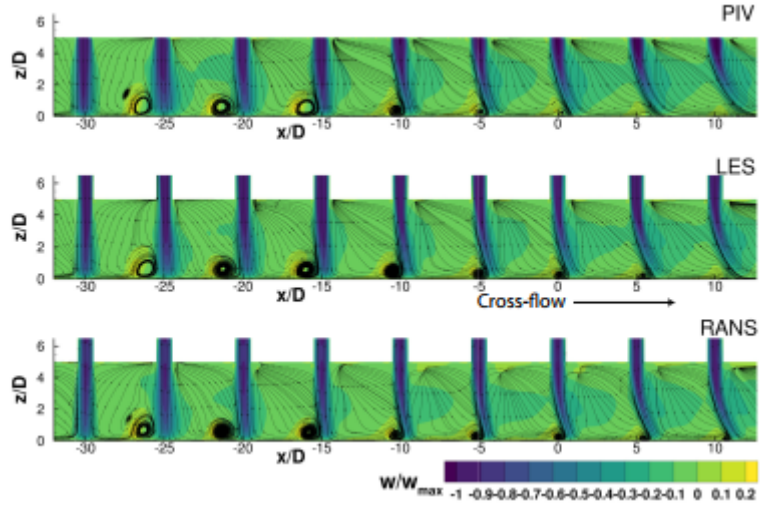


Figure C.2: Mean velocity distribution in the mid-plane ( $y = 0$  [58])

## C.3 Results

### C.3.1 Flow Field

#### Velocity Field

Figure C.2 shows the velocity distribution in the mid-plane obtained through the PIV, LES, and RANS simulations. The shear layer and the potential core is visible, indeed, downstream the jet, the potential core starts to decay and allows to form the shear layer. So, the fluid forms the crossflow that affects negatively the static pressure in the channel. Upstream the jets, recirculation zones are formed due to viscous forces, leading to an increasing in the jet centerline velocity. In Figure XX, the flow structures are similar for all cases and so, the simulations are well predicted. The RANS results had a lower deflection jet due to the crossflow compared to LES results.

#### Turbulence Field

The flow structure between the #7 and #8 jet, in the channel along with the vorticity in the direction of crossflow are shown in Figure C.3. The vorticity distribution and

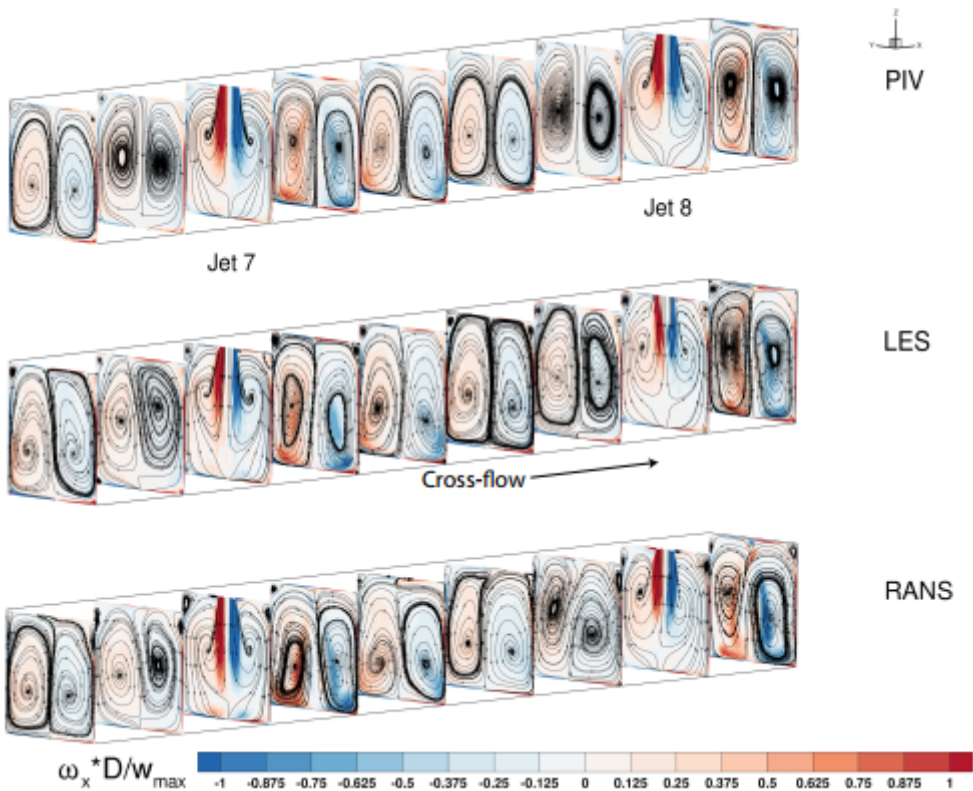


Figure C.3: Vorticity distribution in the direction of crossflow [58]

the secondary flow structures arising from the interaction of the jets with the crossflow are well reproduced in the simulations. We can see that two counter-rotating jets are formed and redirected in the channel. Downstream of the jets, the vorticity intensity increases. As the jet meets the crossflow, it increases the kinetic energy, and so the values of the vorticity increase. However, between the two jets, we notice that the values of the vorticity reduce. As soon as the jet impinges the target, the shear layer of the wall jet is formed due to the viscous forces. Thus, the thickness of the wall jet increases with the fluid moved along the walls; and reduces the vortices. Compared to the PIV, the magnitude of the vorticity is slightly higher in the shear layers in the shear layer of Jet 7 and 8. Indeed, the production terms due to normal stresses are over-predicted due to turbulence models.

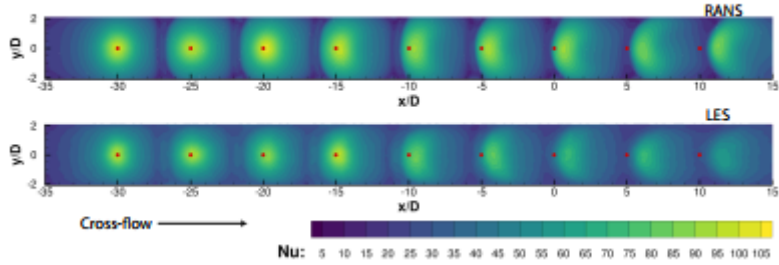


Figure C.4: Nusselt number distribution on the heated plate, the red dots indicate geometric jet centers

### C.3.2 Heat transfer

The Nusselt number allows to evaluate the heat transfer distribution on the heated plate. The distribution obtained through the RANS and LES simulations are presented in Figure XXX. High Nusselt number corresponds to the stagnation point where the jet is hitting the surface with a temperature close to the plenum temperature  $T_{ref}$ . Indeed, this point correspond the end of the potential core and the arrival of turbulence from the shear layer. Convective transfer dominates over conductive transfer, so the heat transfer is higher due to the turbulence created by the crossflow. Around the stagnation point, the Nusselt Numbers decreases because the wall jet is developed and the viscous forces affected negatively the Nusselt number. The shape of the Nusselt number contour changes from circular to oval due to the jet deviation. The crossflow generated two aspects: firstly an increase turbulence in the jet centerline, and secondly an improvement of the heat transfer. However, in the wall jet region, the flow is accelerated, and so the high crossflow velocities reduce progressively the Nusselt number because the spent fluid is entrained into the jets in the radial direction. For the RANS simulations, the heat transfer rates are over-predicted especially in the stagnation regions. This deviation is generated due to the higher turbulence field and the lesser deflection jet presented in Section XXX. The behavior of the distribution is similar for the two cases, but the LES results are smeared. This could be due to the decrease of turbulence in wall jet region in RANS results, resulting in more pronounced extrema in the distribution.

## C.4 Validation

For validation of my smooth configuration, I realised a comparison between different geometrical setup such as CFD solver and grid. Indeed, the smooth configuration that I used is not similar to Tabassum configuration. In this particular setup, the iteration number is slightly different. My simulations have only 50,000 iterations in opposition to Tabassum simulation with 80,000 iterations. However, this factor can have secondary effects. Indeed, an iteration is a numerical sweep through the entire model and the results change a lot from one iteration to the next. Figure C.5 shows the spanwise averaged Nusselt number for the Tabassum data and my results. The peaks of the Nusselt number correspond to the jet stagnation regions, where there is a high deviation and a high heat transfer. ((The maximum of the Nusselt number is 81 for the jet #3, and from the jet #5, the Nusselt number maxima decreases as figure XXX shows because the crossflow becomes dominating on downstream the jet #4. Indeed, the crossflow velocities reduce progressively the Nusselt number.)) From the jet #5, the averaged Nusselt number reduces progressively due to the crossflow. Indeed, the velocity of the crossflow increases along the channel and can affect negatively the heat transfer. The behaviour is similar for the two cases, but for the last jets, there is slightly different due to the iteration number. Despite this small difference, the results have a good agreement with Tabassum data.

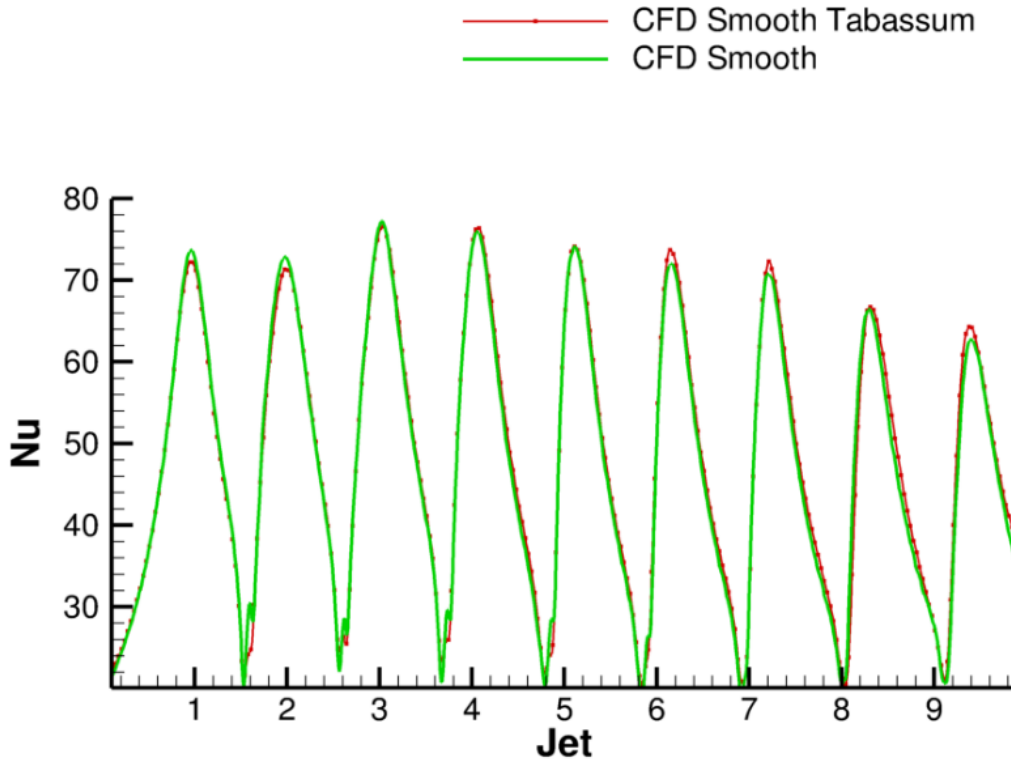


Figure C.5: Validation Smooth DLR with Tabassum data

## C.5 Conclusion

The comparisons provided some uncertainties in the heat transfer and turbulence field. The concluded points of the study are:

- The velocity fields are well predicted in the simulations and a good agreement with experience data.
- The RANS results show lesser deviations due to the crossflow. This effect contributes to the over-predicted of Nusselt number values in the stagnation points.
- The magnitude of turbulence is not correctly modelled in RANS simulations,

and so enhances the heat transfer.

- Both CFD approaches are in good agreement with the PIV measurements. Regarding the low computational costs, a RANS approach allows to predict correctly the velocity field.
- My CFD results are in good agreement with Tabassum data [58].

# Bibliography

- [1] David Adair, Michael Kirka, and Daniel Ryan. “Additive Manufacture of Prototype Turbine Blades for Hot-Fired Engine Performance Validation Trials”. In: *Volume 6: Ceramics; Controls, Diagnostics, and Instrumentation; Education; Manufacturing Materials and Metallurgy*. ASME Turbo Expo 2019: Turbomachinery Technical Conference and Exposition. Phoenix, Arizona, USA: American Society of Mechanical Engineers, June 17, 2019, V006T24A012. ISBN: 978-0-7918-5867-7. DOI: 10.1115/GT2019-90966. URL: <https://asmedigitalcollection.asme.org/GT/proceedings/GT2019/58677/Phoenix,%20Arizona,%20USA/1066988> (visited on 12/17/2021).
- [2] AMCM. *AMCM M 4K: Large Scale, High Productivity System for Demanding AM Applications. 1 Meter Building Height with up to 4 x 1,000 W Laser Power.* URL: <https://amcm.com/machines/amcm-m4k> (visited on 01/04/2023).
- [3] Mats O. Annerfeldt, Johan L. Persson, and Tord Torisson. “Experimental Investigation of Impingement Cooling With Turbulators or Surface Enlarging Elements”. In: *Volume 3: Heat Transfer; Electric Power; Industrial and Co-generation*. ASME Turbo Expo 2001: Power for Land, Sea, and Air. New Orleans, Louisiana, USA: American Society of Mechanical Engineers, June 4, 2001, V003T01A032. ISBN: 978-0-7918-7852-1. DOI: 10.1115/2001-GT-0149. URL: <https://asmedigitalcollection.asme.org/GT/proceedings/GT2001/78521/New%20rleans,%20Louisiana,%20USA/249914> (visited on 12/16/2022).
- [4] ArianeGroup. *Future Ariane Propulsion Module Simplified: Simplified by Additive Manufacturing*. Feb. 2019. URL: [https://www.eos.info/01\\_parts-and-](https://www.eos.info/01_parts-and-)

- [applications/case\\_studies\\_applications\\_parts/\\_case\\_studies\\_pdf/en\\_cases/cs\\_m\\_aerospace\\_arianegroup\\_en.pdf](https://www.arianegroup.com/en/cases/cs_m_aerospace_arianegroup_en.pdf) (visited on 01/03/2023).
- [5] Mohamed Balbaa et al. “On Selective Laser Melting of Inconel 718: Densification, Surface Roughness, and Residual Stresses”. In: *Materials & Design* 193 (Aug. 2020), p. 108818. ISSN: 02641275. DOI: 10.1016/j.matdes.2020.108818. URL: <https://linkinghub.elsevier.com/retrieve/pii/S026412752030352X> (visited on 01/04/2023).
  - [6] Abdmonem H. Beitelmal, Michel A. Saad, and Chandrakant D. Patel. “Effects of Surface Roughness on the Average Heat Transfer of an Impinging Air Jet”. In: *International Communications in Heat and Mass Transfer* 27.1 (Jan. 2000), pp. 1–12. ISSN: 07351933. DOI: 10.1016/S0735-1933(00)00079-8. URL: <https://linkinghub.elsevier.com/retrieve/pii/S0735193300000798> (visited on 12/20/2022).
  - [7] Robin G Brakmann. *Increasing Heat Transfer in Convective Cooling Systems with Optimized Surface Structures*. Verlag Dr. Hut, 2017.
  - [8] Robin G. Brakmann et al. “Experimental and Numerical Heat Transfer Investigation of an Impinging Jet Array on a Target Plate Roughened by Cubic Micro Pin Fins”. In: *Journal of Turbomachinery* 138.11 (Nov. 1, 2016), p. 111010. ISSN: 0889-504X, 1528-8900. DOI: 10.1115/1.4033670. URL: <https://asmedigitalcollection.asme.org/turbomachinery/article/doi/10.1115/1.4033670/378624/Experimental-and-Numerical-Heat-Transfer> (visited on 01/04/2023).
  - [9] J. Brommer. “Numerische Untersuchung des Wärmeübergangs und des Strömungsfeldes eines Prall-strahlfeldes in Kombination mit V-Rippen auf der Prallplatte”. PhD thesis. University of Stuttgart, Germany, 2016.
  - [10] S. Caliskan and S. Baskaya. “Experimental Investigation of Impinging Jet Array Heat Transfer from a Surface with V-shaped and Convergent-Divergent Ribs”. In: *International Journal of Thermal Sciences* 59 (Sept. 2012), pp. 234–246. ISSN: 12900729. DOI: 10.1016/j.ijthermalsci.2012.04.013. URL: <https://linkinghub.elsevier.com/retrieve/pii/S1290072912001305> (visited on 12/19/2022).

- [11] Ismail Celik et al. “Procedure for Estimation and Reporting of Uncertainty Due to Discretization in CFD Applications”. In: *Journal of Fluids Engineering* 130.7 (2008), p. 078001. ISSN: 00982202. DOI: 10.1115/1.2960953. URL: <http://FluidsEngineering.asmedigitalcollection.asme.org/article.aspx?articleid=1434171> (visited on 11/23/2021).
- [12] Centaur. *Centaur*. 2023. URL: <https://www.centaursoft.com> (visited on 01/04/2023).
- [13] W.M. Chakroun, A.A. Abdel-Rahman, and S.F. Al-Fahed. “Heat Transfer Augmentation for Air Jet Impinged on a Rough Surface”. In: *Applied Thermal Engineering* 18.12 (Dec. 1998), pp. 1225–1241. ISSN: 13594311. DOI: 10.1016/S1359-4311(97)00100-2. URL: <https://linkinghub.elsevier.com/retrieve/pii/S1359431197001002> (visited on 07/15/2022).
- [14] Lingling Chen et al. “Experimental and Numerical Heat Transfer Investigation of an Impingement Jet Array with V-ribs on the Target Plate and on the Impingement Plate”. In: *International Journal of Heat and Fluid Flow* 68 (Dec. 2017), pp. 126–138. DOI: 10.1016/j.ijheatfluidflow.2017.09.005.
- [15] Lingling Chen et al. “Experimental and numerical heat transfer investigation of an impingement jet array with V-ribs on the target plate and on the impingement plate”. In: *International Journal of Heat and Fluid Flow* 68 (Dec. 2017), pp. 126–138. DOI: 10.1016/j.ijheatfluidflow.2017.09.005.
- [16] the German Aerospace Center DLR. “COMPUTE BEFORE FLIGHT: How the virtual engine can advance aeronautics research”. In: *DLR Magazine* 27.70 (2022), p. 24.
- [17] Sandip Dutta. “Impingement Insert”. U.S. pat. 10494948B2.
- [18] Sandip Dutta and Prashant Singh. “Impingement Heat Transfer Innovations and Enhancements: A Discussion on Selected Geometrical Features”. In: *Volume 5B: Heat Transfer*. ASME Turbo Expo 2021: Turbomachinery Technical Conference and Exposition. Virtual, Online: American Society of Mechanical Engineers, June 7, 2021, V05BT15A011. ISBN: 978-0-7918-8498-0. DOI: 10.1115/GT2021-59394. URL: <https://asmedigitalcollection.asme.org/GT/proceedings/GT2021/84980/V05BT15A011/1120091> (visited on 03/07/2022).

- [19] Brandon Ealy et al. “Characterization of Laser Additive Manufacturing-Fabricated Porous Superalloys for Turbine Components”. In: *Journal of Engineering for Gas Turbines and Power* 139.10 (Oct. 1, 2017), p. 102102. ISSN: 0742-4795, 1528-8919. DOI: 10.1115/1.4035560. URL: <https://asmedigitalcollection.asme.org/gasturbinespower/article/doi/10.1115/1.4035560/373547/Characterization-of-Laser-Additive> (visited on 01/04/2023).
- [20] Energy Education. *Gas Turbine*. 2015. URL: [https://energyeducation.ca/encyclopedia/Gas\\_turbine](https://energyeducation.ca/encyclopedia/Gas_turbine).
- [21] EOS. *Material Data Sheet - EOS NickelAlloy IN718 - M290*. 2021. URL: <https://www.eos.info/de/additive-fertigung/3d-druck-metall/eos-metall-werkstoffe-dmls/nickel-alloy-inconel> (visited on 01/05/2023).
- [22] EOS. *Material Data Sheet - EOS NickelAlloy IN939 - M290*. 2021. URL: <https://www.eos.info/de/additive-fertigung/3d-druck-metall/eos-metall-werkstoffe-dmls/nickel-alloy-inconel> (visited on 05/01/2023).
- [23] Andi Eschenbacher. *Crack-Free 3D Printed Parts with IN939*. 2020. URL: <https://app.gotowebinar.com/unified/index.html#/webinar/5100312705178758925/attend/2929305005902512909> (visited on 01/02/2023).
- [24] Lamyaa A. El-Gabry and Deborah A. Kaminski. “Experimental Investigation of Local Heat Transfer Distribution on Smooth and Roughened Surfaces Under an Array of Angled Impinging Jets”. In: *Journal of Turbomachinery* 127.3 (July 1, 2005), pp. 532–544. ISSN: 0889-504X, 1528-8900. DOI: 10.1115/1.1861918. URL: <https://asmedigitalcollection.asme.org/turbomachinery/article/127/3/532/471275/Experimental-Investigation-of-Local-Heat-Transfer> (visited on 03/25/2022).
- [25] Andres Gasser et al. “Laser Additive Manufacturing: Laser Metal Deposition (LMD) and Selective Laser Melting (SLM) in Turbo-Engine Applications”. In: *Laser Technik Journal* 7.2 (Feb. 2010), pp. 58–63. ISSN: 16137728, 18639119. DOI: 10.1002/latj.201090029. URL: <https://onlinelibrary.wiley.com/doi/10.1002/latj.201090029> (visited on 01/04/2023).
- [26] GE. *Concept Laser Mlab Family*. URL: <https://www.ge.com/additive/additive-manufacturing/machines/dmlm-machines/mlab-family> (visited on 01/04/2023).

- [27] LFG Geers et al. “Heat transfer correlation for hexagonal and in-line arrays of impinging jets”. In: *International Journal of Heat and Mass Transfer* 51.21-22 (2008), pp. 5389–5399.
- [28] Georg Geiser et al. “On the Simulation and Spectral Analysis of Unsteady Turbulence and Transition Effects in a Multistage Low Pressure Turbine”. In: *Journal of Turbomachinery* 141.5 (Jan. 2019). 051012. ISSN: 0889-504X. DOI: 10.1115/1.4041820. eprint: [https://asmedigitalcollection.asme.org/turbomachinery/article-pdf/141/5/051012/6311690/turbo\\\_141\\\_05\\\_051012.pdf](https://asmedigitalcollection.asme.org/turbomachinery/article-pdf/141/5/051012/6311690/turbo\_141\_05\_051012.pdf). URL: <https://doi.org/10.1115/1.4041820>.
- [29] Luai AL-Hadhrami, Todd Griffith, and Je-Chin Han. “Heat Transfer in Two-Pass Rotating Rectangular Channels (AR=2) With Five Different Orientations of 45 Deg V-Shaped Rib Turbulators”. In: *Journal of Heat Transfer* 125.2 (Apr. 1, 2003), pp. 232–242. ISSN: 0022-1481, 1528-8943. DOI: 10.1115/1.1561455. URL: <https://asmedigitalcollection.asme.org/heattransfer/article/125/2/232/444463/Heat-Transfer-in-TwoPass-Rotating-Rectangular> (visited on 05/17/2022).
- [30] L.G. Hansen and B.W. Webb. “Air Jet Impingement Heat Transfer from Modified Surfaces”. In: *International Journal of Heat and Mass Transfer* 36.4 (Mar. 1993), pp. 989–997. ISSN: 00179310. DOI: 10.1016/S0017-9310(05)80283-2. URL: <https://linkinghub.elsevier.com/retrieve/pii/S0017931005802832> (visited on 12/20/2022).
- [31] Andrea Ianiro and Gennaro Cardone. “Heat Transfer Rate and Uniformity in Multichannel Swirling Impinging Jets”. In: *Applied Thermal Engineering* 49 (Dec. 2012), pp. 89–98. ISSN: 13594311. DOI: 10.1016/j.applthermaleng.2011.10.018. URL: <https://linkinghub.elsevier.com/retrieve/pii/S135943111005564> (visited on 04/22/2022).
- [32] S.A. Isaev et al. “Numerical Simulation of the Turbulent Air Flow in the Narrow Channel with a Heated Wall and a Spherical Dimple Placed on It for Vortex Heat Transfer Enhancement Depending on the Dimple Depth”. In: *International Journal of Heat and Mass Transfer* 94 (Mar. 2016), pp. 426–448. ISSN: 00179310. DOI: 10.1016/j.ijheatmasstransfer.2015.11.002. URL:

<https://linkinghub.elsevier.com/retrieve/pii/S0017931015306979> (visited on 12/20/2022).

- [33] Nicholas M. R. Jeffers et al. “Heat Transfer From Novel Target Surface Structures to a Normally Impinging, Submerged and Confined Water Jet”. In: *Journal of Thermal Science and Engineering Applications* 1.3 (Sept. 1, 2009), p. 031001. ISSN: 1948-5085, 1948-5093. DOI: 10.1115/1.4000564. URL: <https://asmedigitalcollection.asme.org/thermalscienceapplication/article/doi/10.1115/1.4000564/464096/Heat-Transfer-From-Novel-Target-Surface-Structures> (visited on 12/14/2021).
- [34] K. Kanokjaruvijit and R. F. Martinez-Botas. “Heat Transfer and Pressure Investigation of Dimple Impingement”. In: *Journal of Turbomachinery* 130.1 (Jan. 1, 2008), p. 011003. ISSN: 0889-504X, 1528-8900. DOI: 10.1115/1.2220048. URL: <https://asmedigitalcollection.asme.org/turbomachinery/article/doi/10.1115/1.2220048/462410/Heat-Transfer-and-Pressure-Investigation-of-Dimple> (visited on 12/20/2022).
- [35] M. Karmuhilan and Somasundaram Kumanan. “A Review on Additive Manufacturing Processes of Inconel 625”. In: *Journal of Materials Engineering and Performance* 31.4 (Apr. 2022), pp. 2583–2592. ISSN: 1059-9495, 1544-1024. DOI: 10.1007/s11665-021-06427-3. URL: <https://link.springer.com/10.1007/s11665-021-06427-3> (visited on 01/04/2023).
- [36] M. Kato and Brian Launder. “The Modelling of Turbulent Flow around Stationary and Vibrating Square Cylinders”. In: (Jan. 1993).
- [37] Sang Hyouk Kim, Hyun Dong Kim, and Kyung Chun Kim. “Measurement of Two-Dimensional Heat Transfer and Flow Characteristics of an Impinging Sweeping Jet”. In: *International Journal of Heat and Mass Transfer* 136 (June 2019), pp. 415–426. ISSN: 00179310. DOI: 10.1016/j.ijheatmasstransfer.2019.03.021. URL: <https://linkinghub.elsevier.com/retrieve/pii/S0017931018359568> (visited on 04/22/2022).
- [38] Seon Ho Kim et al. “Uniform Impingement Heat Transfer Distribution in Corrugated Channel with an Anti-Crossflow-Wing”. In: *International Journal of Heat and Mass Transfer* 201 (Feb. 2023), p. 123576. ISSN: 00179310. DOI: 10.

- 1016/j.ijheatmasstransfer.2022.123576. URL: <https://linkinghub.elsevier.com/retrieve/pii/S0017931022010456> (visited on 12/20/2022).
- [39] K Knowles and M Myszko. “Turbulence measurements in radial wall-jets”. In: *Experimental Thermal and Fluid Science* 17.1-2 (1998), pp. 71–78.
- [40] Robin B. Langtry and Florian R. Menter. “Correlation-Based Transition Modeling for Unstructured Parallelized Computational Fluid Dynamics Codes”. In: *AIAA Journal* 47.12 (Dec. 2009), pp. 2894–2906. ISSN: 0001-1452, 1533-385X. DOI: 10.2514/1.42362. URL: <https://arc.aiaa.org/doi/10.2514/1.42362> (visited on 01/04/2023).
- [41] D. A. Lesyk et al. “Porosity and Surface Defects Characterization of Hot Isostatically Pressed Inconel 718 Alloy Turbine Blades Printed by 3D Laser Metal Fusion Technology”. In: *MRS Advances* 7.9 (Apr. 2022), pp. 197–201. ISSN: 2059-8521. DOI: 10.1557/s43580-021-00187-x. URL: <https://link.springer.com/10.1557/s43580-021-00187-x> (visited on 01/03/2023).
- [42] D. A. Lesyk et al. “Surface Shot Peening Post-processing of Inconel 718 Alloy Parts Printed by Laser Powder Bed Fusion Additive Manufacturing”. In: *Journal of Materials Engineering and Performance* 30.9 (Sept. 2021), pp. 6982–6995. ISSN: 1059-9495, 1544-1024. DOI: 10.1007/s11665-021-06103-6. URL: <https://link.springer.com/10.1007/s11665-021-06103-6> (visited on 01/03/2023).
- [43] Dmytro A. Lesyk et al. “Additive Manufacturing of the Superalloy Turbine Blades by Selective Laser Melting: Surface Quality, Microstructure and Porosity”. In: *New Technologies, Development and Application III*. Ed. by Isak Karabegović. Vol. 128. Lecture Notes in Networks and Systems. Cham: Springer International Publishing, 2020, pp. 267–275. ISBN: 978-3-030-46816-3 978-3-030-46817-0. DOI: 10.1007/978-3-030-46817-0\_30. URL: [http://link.springer.com/10.1007/978-3-030-46817-0\\_30](http://link.springer.com/10.1007/978-3-030-46817-0_30) (visited on 01/04/2023).
- [44] Liubov Magerramova, Boris Vasilyev, and Vladimir Kinzburskiy. “Novel Designs of Turbine Blades for Additive Manufacturing”. In: *Volume 5C: Heat Transfer*. ASME Turbo Expo 2016: Turbomachinery Technical Conference and Exposition. Seoul, South Korea: American Society of Mechanical Engineers, June 13, 2016, V05CT18A001. ISBN: 978-0-7918-4980-4. DOI: 10.1115/GT2016-

56084. URL: <https://asmedigitalcollection.asme.org/GT/proceedings/GT2016/49804/Seoul,%20South%20Korea/239676> (visited on 01/24/2022).
- [45] Holger Martin. “Heat and Mass Transfer between Impinging Gas Jets and Solid Surfaces”. In: *Advances in Heat Transfer*. Vol. 13. Elsevier, 1977, pp. 1–60. ISBN: 978-0-12-020013-9. DOI: 10.1016/S0065-2717(08)70221-1. URL: <https://linkinghub.elsevier.com/retrieve/pii/S0065271708702211> (visited on 03/18/2022).
- [46] Holger Martin. “Heat and mass transfer between impinging gas jets and solid surfaces”. In: *Advances in heat transfer*. Vol. 13. Elsevier, 1977, pp. 1–60.
- [47] Florian R. Menter, M. Kuntz, and Robin B. Langtry. “Ten Years of Industrial Experience with the SST Turbulence Model”. In: *Heat and Mass Transfer 4* (Jan. 2003).
- [48] Carosena Meola. “A new correlation of Nusselt number for impinging jets”. In: *Heat Transfer Engineering* 30.3 (2009), pp. 221–228.
- [49] Nicholas Miller et al. “Effects of Jet Diameter and Surface Roughness on Internal Cooling With Single Array of Jets”. In: *Volume 3A: Heat Transfer*. ASME Turbo Expo 2013: Turbine Technical Conference and Exposition. San Antonio, Texas, USA: American Society of Mechanical Engineers, June 3, 2013, V03AT12A038. ISBN: 978-0-7918-5514-0. DOI: 10.1115/GT2013-95400. URL: <https://asmedigitalcollection.asme.org/GT/proceedings/GT2013/55140/San%20Antonio,%20Texas,%20USA/247447> (visited on 12/16/2022).
- [50] Kevin Minet et al. “Superalloys, Powders, Process Monitoring in Additive Manufacturing”. In: *Additive Manufacturing for the Aerospace Industry*. Elsevier, 2019, pp. 163–185. ISBN: 978-0-12-814062-8. DOI: 10.1016/B978-0-12-814062-8.00009-1. URL: <https://linkinghub.elsevier.com/retrieve/pii/B9780128140628000091> (visited on 01/03/2023).
- [51] AK Mohanty and AA Tawfek. “Heat transfer due to a round jet impinging normal to a flat surface”. In: *International Journal of Heat and Mass Transfer* 36.6 (1993), pp. 1639–1647.
- [52] Nitin P. Padture. “Advanced Structural Ceramics in Aerospace Propulsion”. In: *Nature Materials* 15.8 (Aug. 2016), pp. 804–809. ISSN: 1476-1122, 1476-4660.

- DOI: 10.1038/nmat4687. URL: <http://www.nature.com/articles/nmat4687> (visited on 12/20/2021).
- [53] Dong Ho Rhee, Yong Woo Nam, and Hyung Hee Cho. “Local Heat/Mass Transfer With Various Rib Arrangements in Impingement/Effusion Cooling System With Crossflow”. In: *Journal of Turbomachinery* 126.4 (Oct. 1, 2004), pp. 615–626. ISSN: 0889-504X, 1528-8900. DOI: 10.1115/1.1791287. URL: <https://asmedigitalcollection.asme.org/turbomachinery/article/126/4/615/447608/Local-HeatMass-Transfer-With-Various-Rib> (visited on 12/16/2022).
  - [54] Rolls Royce. *The jet engine*. John Wiley & Sons, 2015.
  - [55] Siemens. *Success Story Siemens 3D Printing for Gas Turbine Blade*. URL: <https://www.eos.info/en/all-3d-printing-applications/production-and-industry/turbomachinery-turbines> (visited on 04/29/2022).
  - [56] Jacob C. Snyder and Karen A. Thole. “Tailoring Surface Roughness Using Additive Manufacturing to Improve Internal Cooling”. In: *Journal of Turbomachinery* 142.7 (July 1, 2020), p. 071004. ISSN: 0889-504X, 1528-8900. DOI: 10.1115/1.4047380. URL: <https://asmedigitalcollection.asme.org/turbomachinery/article/142/7/071004/1084157/Tailoring-Surface-Roughness-Using-Additive> (visited on 01/24/2022).
  - [57] Sadiya Tabassum et al. “Assessment of Computational Fluid Dynamic Modeling of Multi-Jet Impingement Cooling and Validation With the Experiments”. In: *Volume 6B: Heat Transfer*. ASME Turbo Expo 2022: Turbomachinery Technical Conference and Exposition. Rotterdam, Netherlands: American Society of Mechanical Engineers, June 13, 2022, V06BT15A011. ISBN: 978-0-7918-8604-5. DOI: 10.1115/GT2022-81749. URL: <https://asmedigitalcollection.asme.org/GT/proceedings/GT2022/86045/V06BT15A011/1148927> (visited on 01/05/2023).
  - [58] Sadiya Tabassum et al. “Assessment of Computational Fluid Dynamic Modeling of Multi-Jet Impingement Cooling and Validation With the Experiments”. In: *Turbo Expo: Power for Land, Sea, and Air* Volume 6B: Heat Transfer — General Interest/Additive Manufacturing Impacts on Heat Transfer; Internal Air

- Systems; Internal Cooling, GT2022-81749 (June 2022). DOI: 10.1115/GT2022-81749.
- [59] Jason Town et al. “State-of-the-Art Cooling Technology for a Turbine Rotor Blade”. In: *Journal of Turbomachinery* 140.7 (July 1, 2018), p. 071007. ISSN: 0889-504X, 1528-8900. DOI: 10.1115/1.4039942. URL: <https://asmedigitalcollection.asme.org/turbomachinery/article/doi/10.1115/1.4039942/369493/StateoftheArt-Cooling-Technology-for-a-Turbine> (visited on 03/25/2022).
- [60] Luigi Ventola et al. “Rough Surfaces with Enhanced Heat Transfer for Electronics Cooling by Direct Metal Laser Sintering”. In: *International Journal of Heat and Mass Transfer* 75 (Aug. 2014), pp. 58–74. ISSN: 00179310. DOI: 10.1016/j.ijheatmasstransfer.2014.03.037. URL: <https://linkinghub.elsevier.com/retrieve/pii/S0017931014002439> (visited on 01/04/2023).
- [61] *Numerical Investigation of Impingement Heat Transfer on a Flat and Square Pin-Fin Roughened Plates*. Vol. Volume 3A: Heat Transfer. Turbo Expo: Power for Land, Sea, and Air. V03AT12A016. June 2013. eprint: <https://asmedigitalcollection.asme.org/GT/proceedings-pdf/GT2013/55140/V03AT12A016/2419819/v03at12a016-gt2013-94473.pdf>. URL: <https://doi.org/10.1115/GT2013-94473>.
- [62] Chenglong Wang, Lei Wang, and Bengt Sundén. “A Novel Control of Jet Impingement Heat Transfer in Cross-Flow by a Vortex Generator Pair”. In: *International Journal of Heat and Mass Transfer* 88 (Sept. 2015), pp. 82–90. ISSN: 00179310. DOI: 10.1016/j.ijheatmasstransfer.2015.04.056. URL: <https://linkinghub.elsevier.com/retrieve/pii/S0017931015004263> (visited on 09/06/2022).
- [63] Chenglong Wang et al. “Effects of Vortex Generators on the Jet Impingement Heat Transfer at Different Cross-Flow Reynolds Numbers”. In: *International Journal of Heat and Mass Transfer* 96 (May 2016), pp. 278–286. ISSN: 00179310. DOI: 10.1016/j.ijheatmasstransfer.2016.01.042. URL: <https://linkinghub.elsevier.com/retrieve/pii/S0017931015303422> (visited on 12/16/2022).
- [64] Chenglong Wang et al. “Heat Transfer and Fluid Flow of a Single Jet Impingement in Cross-Flow Modified by a Vortex Generator Pair”. In: *Volume 5A: Heat*

- Transfer*. ASME Turbo Expo 2016: Turbomachinery Technical Conference and Exposition. Seoul, South Korea: American Society of Mechanical Engineers, June 13, 2016, V05AT13A015. ISBN: 978-0-7918-4978-1. DOI: 10.1115/GT2016-56894. URL: <https://asmedigitalcollection.asme.org/GT/proceedings/GT2016/49781/Seoul,%20South%20Korea/240314> (visited on 12/16/2022).
- [65] Xiaoqing Wang, Xibing Gong, and Kevin Chou. “Review on Powder-Bed Laser Additive Manufacturing of Inconel 718 Parts”. In: *Proceedings of the Institution of Mechanical Engineers, Part B: Journal of Engineering Manufacture* 231.11 (Sept. 2017), pp. 1890–1903. ISSN: 0954-4054, 2041-2975. DOI: 10.1177/0954405415619883. URL: <http://journals.sagepub.com/doi/10.1177/0954405415619883> (visited on 01/04/2023).
- [66] Patrick Wehrel. *Technological Level of CMC Components for Stationary Gas Turbines and Aero-Engines*. Internal Report DLR-IB-AT-KP-2022-32. Köln: DLR, May 23, 2022. URL: <https://elib.dlr.de/186166/>.
- [67] Patrick Wehrel et al. “Performance and Emissions Benefits of Cooled Ceramic Matrix Composite Vanes for High Pressure Turbines”. In: Turbo Expo 2023: Power for Land, Sea and Air. Boston, Massachusetts, USA: American Society of Mechanical Engineers, 2023.
- [68] Bernhard Weigand and Sebastian Spring. “Multiple Jet Impingement - A Review”. In: *Proceedings of International Symposium on Heat Transfer in Gas Turbine Systems*. TURBINE-09. Proceedings of International Symposium on Heat Transfer in Gas Turbine Systems. Antalya, Turkey: Begellhouse, 2009, pp. 1–36. ISBN: 978-1-56700-263-8. DOI: 10.1615/ICHMT.2009.HeatTransfGasTurbSyst.470. URL: <http://www.dl.begellhouse.com/references/1bb331655c289a0a,7383ff5048430c16,568ff06b7952f724.html> (visited on 03/18/2022).
- [69] Bernhard Weigand and Sebastian Spring. “Multiple jet impingement- a review”. In: *TURBINE-09. Proceedings of International Symposium on Heat Transfer in Gas Turbine Systems*. Begel House Inc. 2009.
- [70] Mao-Yu Wen and Kuen-Jang Jang. “An impingement cooling on a flat surface by using circular jet with longitudinal swirling strips”. In: *International Journal of Heat and Mass Transfer* 46.24 (2003), pp. 4657–4667.

- [71] Xin Wen et al. “Interaction of Dual Sweeping Impinging Jets at Different Reynolds Numbers”. In: *Physics of Fluids* 30.10 (Oct. 2018), p. 105105. ISSN: 1070-6631, 1089-7666. DOI: 10.1063/1.5054161. URL: <http://aip.scitation.org/doi/10.1063/1.5054161> (visited on 04/22/2022).
- [72] Lesley M Wright and Je-Chin Han. “Enhanced internal cooling of turbine blades and vanes”. In: *The gas turbine handbook* 4 (2006), pp. 1–5.
- [73] Yunfei Xing and Bernhard Weigand. “Experimental Investigation of Impingement Heat Transfer on a Flat and Dimpled Plate with Different Crossflow Schemes”. In: *International Journal of Heat and Mass Transfer* 53.19-20 (Sept. 2010), pp. 3874–3886. ISSN: 00179310. DOI: 10.1016/j.ijheatmasstransfer.2010.05.006. URL: <https://linkinghub.elsevier.com/retrieve/pii/S0017931010002401> (visited on 01/04/2023).
- [74] Liang Xu et al. “Flow and Heat Transfer Characteristics of a Swirling Impinging Jet Issuing from a Threaded Nozzle”. In: *Case Studies in Thermal Engineering* 25 (June 2021), p. 100970. ISSN: 2214157X. DOI: 10.1016/j.csite.2021.100970. URL: <https://linkinghub.elsevier.com/retrieve/pii/S2214157X21001337> (visited on 04/21/2022).
- [75] W.M. Yan et al. “Experimental Study of Impinging Heat Transfer along Rib-Roughened Walls by Using Transient Liquid Crystal Technique”. In: *International Journal of Heat and Mass Transfer* 48.12 (June 2005), pp. 2420–2428. ISSN: 00179310. DOI: 10.1016/j.ijheatmasstransfer.2004.12.048. URL: <https://linkinghub.elsevier.com/retrieve/pii/S0017931005001018> (visited on 12/16/2022).
- [76] N Zuckerman and N Lior. “Jet impingement heat transfer: physics, correlations, and numerical modeling”. In: *Advances in heat transfer* 39 (2006), pp. 565–631.
- [77] N. Zuckerman and N. Lior. “Jet Impingement Heat Transfer: Physics, Correlations, and Numerical Modeling”. In: *Advances in Heat Transfer*. Elsevier, 2006, pp. 565–631. DOI: 10.1016/s0065-2717(06)39006-5.